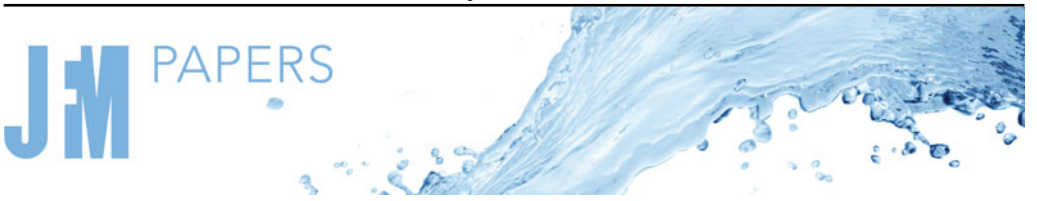
J. Fluid Mech. (2026), *vol.* 1046, A53, doi:10.1017/jfm.2026.12218



Fluid–structure interaction in a square array of submerged flexible stems

Weilin Chen[1] **and Yuzhu Pearl Li**[1]

[1]Department of Civil and Environmental Engineering, National University of Singapore, Singapore 117576, Republic of Singapore

Corresponding author: Yuzhu Pearl Li, pearl.li@nus.edu.sg

(Received 23 March 2026 UTC; revised 9 August 2026 UTC; accepted 21 September 2026 UTC)

The evolution of flow structure is fundamental to establishing an accurate framework for predicting turbulent energy dissipation, momentum transfer, and sediment and nutrient transport within and above flexible stem arrays. The dynamics of flexible stems plays a crucial role in shaping these physical features. In this paper, direct numerical simulations are performed to examine flow through a three-dimensional square array of flexible stems, with explicit consideration of flexibility (K) effects. The results provide a comprehensive characterisation of the coupled stem dynamics, flow distribution and vortex structures. Three distinct dynamical regimes are identified. For large K, the stems behave as nearly rigid, causing the flow to accelerate through the gaps while attenuating behind the stems. At intermediate K, a perfect lock-in occurs between the stem's natural and oscillation frequencies, leading to large-amplitude vibrations and markedly altered flow characteristics. For small K, the oscillation amplitude decreases but deformation increases, producing irregular stem dynamics and complex flow features. The flow dynamics underlying these regimes is systematically elucidated. Furthermore, energy dissipation and sediment transport effects are quantified through hydrodynamic drag, bed shear stress, and root mean square bed shear friction distributions. The array with intermediate K exhibits the highest energy dissipation efficiency, surpassing even the rigid configuration. The bed shear stress reaches a peak at the upstream edge of the array, whereas stem oscillation redistributes the flow momentum towards the upper canopy and the overlying flow, reducing velocity fluctuations near the bed. Finally, the mechanisms governing the structural dynamics and hydrodynamic forces are discussed in detail. This study offers new physical insights into flow–structure interactions within flexible stem arrays, and proposes an optimised strategy for improving energy dissipation in coastal protection applications.

Key words: flow-structure interactions, vortex dynamics, vortex interactions

© The Author(s), 2026. Published by Cambridge University Press. This is an Open Access article, distributed under the terms of the Creative Commons Attribution licence (https://creativecommons.org/licenses/by/4.0/), which permits unrestricted re-use, distribution and reproduction, provided the original article is properly cited.

https://doi.org/10.1017/jfm.2026.12218 Published online by Cambridge University Press

1. Introduction

Wall-mounted flexible structures, such as seagrasses, mangroves, kelps, forests and coral reefs, are ubiquitous in natural aquatic environments, and play crucial roles in ecosystem functioning (Carpenter & Lodge 1986; Green & Short 2003; Unsworth *et al.* 2022). Aquatic vegetation provides habitats and regulates oxygen, carbon and nutrient cycling (Wilcock *et al.* 1999; Schulz *et al.* 2003). Within vegetated meadows, nutrients and sediments tend to be retained and deposited, potentially improving water quality, supplying food sources for aquatic organisms, and contributing to bed stabilisation (Carpenter & Lodge 1986; Sand-Jensen 1998). From an engineering and environmental perspective, submerged canopies are also effective in attenuating wave energy and modulating sediment transport, contributing to coastal stability (Day *et al.* 2007; Temmerman *et al.* 2013). However, despite their ecological and hydrodynamic importance, the coupled dynamics between vegetation motion and surrounding flow structures remains insufficiently understood. The underlying physical mechanisms depend strongly on vegetation properties and spatial arrangements (Jackson & Winant 1983; Finnigan 2000; Rominger & Nepf 2011). Accurate characterisation of flow–structure interactions (FSIs) within submerged canopies requires spatially and temporally resolved measurements of the in-canopy flow, vegetation motion and associated hydrodynamic forces, which are inherently difficult to obtain experimentally. High-fidelity numerical simulation therefore serves as a powerful tool to resolve the coupled fluid and structural dynamics.

The flow characteristics within and above rigid vegetation canopies are governed by their geometric configuration and structural properties (Nepf 2012). The canopy geometry is characterised by the solid volume fraction (ϕ) occupied by canopy elements. When the element is a circular cylinder, $\phi \approx 0.25\pi d^2/D^2$, where d and D denote the vegetation diameter and array width, respectively (Nepf 2012; Nicholas *et al.* 2022). Based on ϕ, the value of which varies with vegetation morphology, canopies are categorised as sparse, dense and transitional (Belcher *et al.* 2003; Coceal & Belcher 2004; Nepf 2012). Sparse canopies resemble rough-wall boundary layers without velocity inflection (Poggi *et al.* 2004; Nepf *et al.* 2007), whereas dense canopies develop two inflection points associated with enhanced shear layers (Nepf 2012). Transitional canopies exhibit a single inflection point that separates the flow into inner- and outer-layer regions. The inner region ($z/h \ll 1$) is dominated by a von Kármán vortex street, while the outer layer ($z/h > 2$) behaves like a rough-wall boundary layer. Between them, a turbulent mixing layer develops at the inflection point, where Kelvin–Helmholtz (K–H) instabilities generate large-scale spanwise vortices (Nicholas *et al.* 2022).

Flexible vegetation exhibits additional complexity due to FSI (Sriram *et al.* 2023). The dynamic responses depend strongly on flexibility, density and morphology (Kim *et al.* 2024). Flexibility is commonly expressed as $K = EI/0.5\rho d h^3 U_{ref}^2$, where E is Young's modulus, I is the cross-sectional momentum of inertia, ρ is the fluid density, d is the side length or diameter, and U_{ref} is the reference velocity. Flexibility affects flow instability in two competing ways (Wong *et al.* 2020): (i) reconfiguration of vegetation reduces drag and stabilises the flow, whereas (ii) the decoupling of fluid and structural perturbations may enhance instability. Depending on flexibility, canopy motion ranges from rigid to strongly prone state, with 'monami' representing coherent waving induced by K–H vortices (Ackerman & Okubo 1993; Carollo *et al.* 2005; Okamoto *et al.* 2016). Subsequent studies (Tschisgale *et al.* 2021; Wang *et al.* 2022*a*; Monti *et al.* 2023; Ni *et al.* 2023; Ni *et al.* 2025) demonstrated that monami persists across a range of flexibilities and primarily arises from large-scale turbulent fluctuations near the canopy top.

https://doi.org/10.1017/jfm.2026.12218 Published online by Cambridge University Press

Flow within vegetated canopies contains both canopy-scale and stem-scale vortices. The shear and velocity inflection at the canopy top trigger K–H instabilities that generate large coherent vortices (Raupach *et al.* 1996; Ghisalberti & Nepf 2002; Singh *et al.* 2016; Wong *et al.* 2020; Vieira *et al.* 2023). These vortices enhance turbulent mixing and vertical momentum transport, promoting the intrusion of Reynolds shear stress into the canopy interior, and modifying the in-canopy flow dynamics (Ghisalberti & Nepf 2006; Wu *et al.* 2023). Stem-scale vortices, by contrast, form in the wake of individual elements (Nepf & Vivoni 2000; Ghisalberti & Nepf 2009; Nepf 2012; He *et al.* 2022).

The velocity distribution within canopies is also influenced by vegetation arrangement, height and density. Flow development proceeds from an adjustment region, where the velocity decays exponentially from the canopy edge (Chen *et al.* 2013), to a fully developed regime characterised by equilibrium between drag and turbulence production (Belcher *et al.* 2003; Rominger & Nepf 2011; Lei & Nepf 2021; Zhang *et al.* 2024). While models for rigid canopies are well validated, the modulation of velocity and turbulence by stem flexibility, particularly for highly deformable vegetation, remains insufficiently understood. This gap motivates the present study, which aims to elucidate how vegetation flexibility reshapes flow structures and hydrodynamic forces within and above canopy arrays.

Hydrodynamic forces govern flow resistance, energy dissipation and sediment transport in vegetated flows. The vegetation-induced drag coefficient is commonly defined as $C_d = F_d/0.5\rho U^2 dh$, where F_d is the drag force acting on the vegetation, and U is the flow velocity. Early resistance models rely on empirical bed-stress or Manning-type formulations (Thompson & Roberson 1976; Arcement *et al.* 1988; Kadlec 1990). These models assume energy loss solely through bed stress, and require empirical calibration, limiting their accuracy for vegetated flows. More recent approaches employ a bulk drag coefficient based on bulk or pore velocity (Wu *et al.* 1999; Zhao *et al.* 2013). However, these reference velocities do not fully represent the effective flow acting on the canopy elements because canopy drag depends on resolved FSI; purely experimental estimates remain indirect (Luhar *et al.* 2010; Pujol *et al.* 2013).

The prediction of sediment transport in vegetated flows is equally critical. Traditional formulations (Shields 1936; Einstein 1942; Meyer-Peter & Müller 1948) relate bedload transport to the mean bed shear stress, whereas recent studies have shown that turbulence generated by vegetation substantially enhances sediment mobility (Heathershaw & Thorne 1985; Sumer *et al.* 2003; Diplas *et al.* 2008; Shih & Diplas 2018; Tseng & Tinoco 2021). In vegetated channels, bare-bed models for bed shear stress (τ_b) often produce substantial errors, since bed stress alone does not fully account for vegetation generated turbulence (Zhao & Nepf 2021; Yang *et al.* 2025). Sediment transport can be underestimated by several orders of magnitude when vegetation-induced turbulence is neglected (Yang & Nepf 2018). Both the near-bed shear stress and the turbulent kinetic energy (TKE) should be considered in sediment transport models (Tinoco & Cowen 2013; Tinoco & Coco 2014; Tinoco & Coco 2016; Tinoco & Coco 2018; Armanini & Cavedon 2019; Zhao & Nepf 2021; Wang *et al.* 2023). Numerical simulations additionally enable direct evaluation of both the mean and root mean square (r.m.s.) bed shear stress, providing a quantitative measure of sediment entrainment (Koken & Constantinescu 2021).

Within emergent canopies, turbulence is primarily generated by wakes of individual stems and branches (Nepf 2012). The magnitude and distribution of this vegetation-generated turbulence depend on stem density, local Reynolds number and plant morphology (Yager & Schmeeckle 2013; Shan *et al.* 2020; Xu & Nepf 2020; Zhao & Nepf 2021). In most cases, vegetation-generated turbulence dominates bed-generated shear stress, making it the primary driver of sediment motion (Yang *et al.* 2016; Yang &

https://doi.org/10.1017/jfm.2026.12218 Published online by Cambridge University Press

Nepf 2018; Yang & Nepf 2019). For submerged canopies, however, an additional source of turbulence arises from the drag discontinuity at the canopy top, which induces a stronger shear layer and promotes turbulence production (King *et al.* 2012; Zhang *et al.* 2020). Lateral shear layers are also important because vortices generated near the canopy edges can penetrate towards the bed. As turbulence modulates sediment mobility and energy dissipation, quantifying the role of canopy-generated turbulence remains of both theoretical and practical significance.

Stem reconfiguration alters the effective frontal area, redistributes drag, and modifies turbulence and mixing. Understanding these coupled processes is therefore essential, and forms a central objective of the present study. Despite considerable previous research, simultaneously resolving all relevant quantities, including stem dynamics, wake evolution, flow distribution, sediment transport and energy dissipation, at high spatial and temporal resolution remains challenging. In this work, we conduct direct numerical simulations of flow through a square array of flexible aquatic stems, representing an idealised model of submerged vegetation with uniform diameter and flexibility along the vertical axis. A newly developed numerical framework, combining the immersed boundary method with the vector form intrinsic finite element (VFIFE) method (Chen & Li 2025), is employed. We investigate how vegetation flexibility modulates FSI and hydrodynamics, with objectives to: (i) characterise flow structures above and within flexible arrays; (ii) quantify stem structural responses under hydrodynamic loading; (iii) assess the effects of flexibility on hydrodynamic drag and in-canopy flow redistribution, including bed shear stress and TKE; and (iv) elucidate the physical mechanisms governing structural dynamics and hydrodynamic loading.

The remainder of this paper is organised as follows. Section 2 introduces the numerical methodology and simulation set-up. Section 3 presents the stem dynamics, three-dimensional (3-D) vortex structures, velocity distribution, hydrodynamic forces, bed shear stress and TKE variations with stem flexibility. The underlying mechanisms governing the stem motion and hydrodynamic loading are also discussed in § 4. Section 5 summarises the main findings and implications for coastal protection and sediment transport.

2. Numerical methodology

2.1. *Numerical method*

The numerical simulations in this study were conducted using an in-house computational fluid dynamics code. The governing equations for the incompressible flow are the Navier–Stokes and continuity equations expressed as

$$\frac{\partial \boldsymbol{u}}{\partial t} + (\boldsymbol{u}\cdot\boldsymbol{\nabla})\boldsymbol{u} = -\frac{1}{\rho}\boldsymbol{\nabla} p + \nu\,\nabla^2\boldsymbol{u} + \boldsymbol{f}, \qquad \boldsymbol{\nabla}\cdot\boldsymbol{u} = 0, \tag{2.1}$$

where $\boldsymbol{u}$ is the velocity of the fluid flow, t is time, p is pressure, ρ is the fluid density, ν is the kinematic viscosity, and $\boldsymbol{f}$ is the extra body force that represents the action of the immersed objects on the fluid.

To discretise (2.1), the second-order Adams–Bashforth time scheme and the second-order central difference scheme are applied, which lead to the conservation form

https://doi.org/10.1017/jfm.2026.12218 Published online by Cambridge University Press

$$\boldsymbol{u}^{n+1} = \boldsymbol{u}^n + \delta t \left(\frac{3}{2}\boldsymbol{h}^n - \frac{1}{2}\boldsymbol{h}^{n-1} - \frac{3}{2}\nabla p^n + \frac{1}{2}\nabla p^{n-1} \right) + \boldsymbol{f}^{n+1/2}\delta t, \qquad (2.2)$$
$$\nabla \cdot \boldsymbol{u}^{n+1} = 0,$$

where $\boldsymbol{h} = \nabla \cdot (-\boldsymbol{u}\boldsymbol{u} + \nu(\nabla \boldsymbol{u} + \nabla \boldsymbol{u}^{\mathrm{T}}))$ is composed of the convective and diffusive terms, in which the superscript T indicates the transpose of a matrix. The superscript n indicates the time step. The extra force $\boldsymbol{f}$ is determined by enforcing the velocity-consistency condition $\boldsymbol{U}^{n+1} = \boldsymbol{V}^{n+1}$ on the fluid–structure interface, where $\boldsymbol{U}^{n+1}$ is the interpolated fluid velocity, and $\boldsymbol{V}^{n+1}$ is the update structure velocity. The extra force $\boldsymbol{f}$ is formally evaluated at the time step $n + 1/2$:

$$\boldsymbol{f}^{n+1/2}\delta t = D(\boldsymbol{F}^{n+1/2}) = D\left(\boldsymbol{V}^{n+1} - I\left(u^n + \delta t \left(\frac{3}{2}\boldsymbol{h}^n - \frac{1}{2}\boldsymbol{h}^{n-1} - \frac{3}{2}\nabla p^n + \frac{1}{2}\nabla p^{n-1} \right) \right) \right), \qquad (2.3)$$

where $\boldsymbol{F}$ is the extra body force on the structure. The interpolation and distribution functions I and D, suggested in Peskin (1972), are applied, and are responsible for data transfer between the non-conforming Eulerian and Lagrangian grids.

The dynamics of a wall-mounted flexible stem is simulated using the VFIFE method (Shih *et al.* 2004; Ting *et al.* 2004*a*,*b*, 2012; Ting & Wang 2008). The VFIFE method is an analytical-numerical approach in structural mechanics based on point value representation and vector form theory. By employing a lumped mass matrix, the method ensures that external forces applied at one spatial point do not affect the motion of other points, thereby eliminating the need for constructing stiffness matrices or solving large nonlinear systems. Compared with conventional finite element methods, the VFIFE method effectively handles large deformations, collisions and elastoplastic behaviours, while avoiding common nonlinear issues such as non-convergence and matrix singularity. Based on the point value description, the stem is discretised into a series of spatial nodes connected by beam elements. The motion and deformation of the stem are represented by the displacement of these nodes, each of which follows Newton's second law of motion:

$$\begin{aligned} m\dot{\boldsymbol{V}} + \zeta m\boldsymbol{V} + \boldsymbol{F}^{int} &= \boldsymbol{F}^{ext}, \\ m\dot{\boldsymbol{\omega}} + \zeta m\boldsymbol{\omega} + \boldsymbol{M}^{int} &= \boldsymbol{M}^{ext}, \end{aligned} \qquad (2.4)$$

where m and I are the mass and momentum of inertia matrix of the node, respectively. Here, $\dot{\boldsymbol{V}}$, $\boldsymbol{V}$, $\dot{\boldsymbol{\omega}}$ and $\boldsymbol{\omega}$ are the acceleration, velocity, angular acceleration and angular velocity of the node, respectively, $\boldsymbol{F}^{int}$, $\boldsymbol{F}^{ext}$, $\boldsymbol{M}^{int}$ and $\boldsymbol{M}^{ext}$ are the internal force, external force, internal moment and external moment, respectively, and ζ is the structural damping coefficient, which is zero in the present study. An explicit iterative scheme based on the central difference is adopted to solve (2.4) as follows:

$$\begin{aligned} \boldsymbol{x}^{n+1} &= \Delta t_s^2 \frac{\boldsymbol{F}^{ext} - \boldsymbol{F}^{int}}{m} + 2\boldsymbol{x}^n - \boldsymbol{x}^{n-1}, \\ \boldsymbol{\alpha}^{n+1} &= \Delta t_s^2 \frac{\boldsymbol{M}^{ext} - \boldsymbol{M}^{int}}{m} + 2\boldsymbol{\alpha}^n - \boldsymbol{\alpha}^{n-1}, \\ \boldsymbol{V}^{n+1} &= \frac{\boldsymbol{x}^{n+1} - \boldsymbol{x}^n}{\Delta t_s}, \quad \omega^{n+1} = \frac{\boldsymbol{\alpha}^{n+1} - \boldsymbol{\alpha}^n}{\Delta t_s}, \end{aligned} \qquad (2.5)$$

where $\boldsymbol{x}$, $\boldsymbol{\alpha}$ and t_s represent the node position, rotation angle of the node, and the structural time step, respectively. The temporal trajectory of any node on the stem is described by a set of spatial points, and the process between the spatial points is defined as the path element. Proper division of the path element allows the properties of each node to vary

https://doi.org/10.1017/jfm.2026.12218 Published online by Cambridge University Press

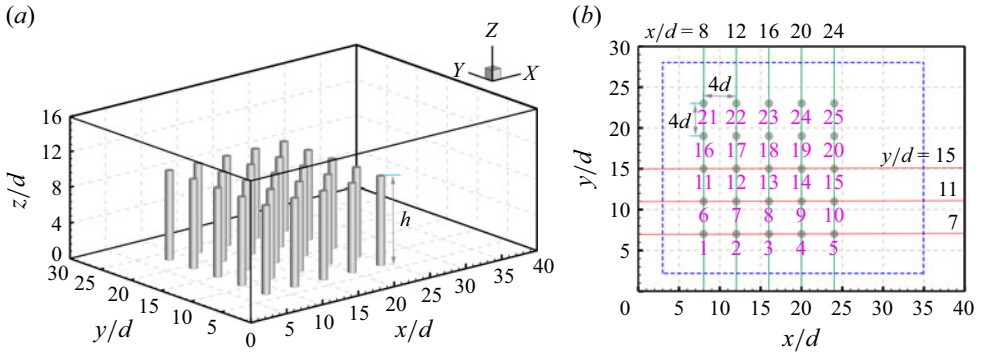


Figure 1. (*a*) Computational domain and (*b*) configuration of the flexible stem array. The array consists of 25 stems arranged in a square array with uniform spacing $4d$ in both the streamwise and transverse directions. Each stem has height-to-diameter ratio $h/d = 10$.

between adjacent elements. Collisions between neighbouring vegetation or between the tip and the wall do not occur, therefore no contact model is employed in the simulations.

2.2. *Simulation set-up for flow through flexible stem arrays*

In the present simulations, a square patch comprising 25 flexible stems is modelled, as shown in figure 1(*a*), representing a short canopy patch (Lei & Nepf 2021). Flow within such a patch remains in the adjustment region, where the streamwise velocity decays from the canopy edge and is generally higher than that in a fully developed region over longer canopies (Chen *et al.* 2013). Each stem has a height of $10d$, and the stems are uniformly spaced $4d$ apart in both the streamwise and transverse directions, as shown in figure 1(*b*). The stem is discretised into 160 beam elements along its height, resulting in 161 circular slices. Each slice is represented by 256 uniformly distributed immersed boundary points (IBPs), ensuring at least one IBP per grid cell, and maintaining adequate spatial resolution. Accordingly, the vertical grid resolution is $\Delta z/d = 1/16$.

The computational domain extends $40d$, $30d$ and $16d$ in the streamwise (x), transverse (y) and vertical (z) directions, respectively. The first stem row is located $8d$ downstream of the inlet, and the lateral clearance between the outer stems and the side boundaries is $7d$, as shown in figure 1(*b*). The upstream distance is selected to allow the imposed inlet condition to adjust before reaching the array. A shorter inlet length may lead to slight variations in the approaching flow. The downstream distance primarily affects the development of the wake and coherent vortical structures near the outlet, whereas its influence on the mean hydrodynamic forces acting on the stems is negligible. Previous domain-independence studies showed that extending the outlet further changes the mean forces by less than 3 % (Chen *et al.* 2015; Chen *et al.* 2022; Tu *et al.* 2018). The submergence ratio (water depth/stem height) is 1.6, corresponding to shallow submergence (Nepf 2012). To cover the potential motion of the stems, a high-resolution uniform mesh covers $32d \times 26d$ in the central region ($3d \leqslant x \leqslant 35d$, $2d \leqslant y \leqslant 28d$), with $\Delta x/d = \Delta y/d = 1/32$, as indicated by the blue rectangle in figure 1(*b*). Outside this zone, a stretched grid is applied to reduce computational costs. The mesh resolution follows the criteria validated in our previous work (Chen & Li 2025). Boundary conditions consist of a Dirichlet inflow ($u = U_\infty$, $v = 0$, $w = 0$), a Neumann outflow ($\partial u/\partial x = 0$, $\partial v/\partial x = 0$, $\partial w/\partial x = 0$), free-slip lateral boundaries ($\partial u/\partial y = 0$, $v = 0$, $\partial w/\partial y = 0$), and a no-slip bottom wall ($u = 0$, $v = 0$, $w = 0$). The free-slip treatment of the upper boundary ($\partial u/\partial z = 0$, $\partial v/\partial z = 0$, $w = 0$) neglects free-surface effects. This approximation is justified because the vortical

https://doi.org/10.1017/jfm.2026.12218 Published online by Cambridge University Press

Parameter	Symbol	Value
Stem number	N	25
Stem diameter	d	1
Stem height	h	10
Array width	D	17
Solid volume fraction	ϕ	0.068
Frontal area per unit array volume	aD	0.294
Stem Reynolds number	Re_d	200
Array Reynolds number	Re_D	1700
Stem flexibility	K	1, 0.32, 0.1, 0.032
Stem Strouhal number	St_d	0.478, 0.253, 0.242, 0.246
Array Strouhal number	St_D	8.126, 4.301, 4.114, 4.182

Table 1. Main geometric and flow parameters of the investigated cases. The array width D is defined as the distance between the outer edges of the outermost stems, i.e. $D = (N-1) \times 4d + d$. The Strouhal number (St) is determined from the dominant frequency of the time series of the spanwise velocity measured in the wake of the array.

structures above the canopy are confined to a limited vertical extent (typically within $3d$ for cases without K–H vortices), which is substantially smaller than the $6d$ clearance between the canopy top and the upper boundary adopted in the present simulations. Saha (2013) demonstrated that for flow over finite wall-mounted cylinders, a clearance exceeding $5d$ is sufficient to eliminate noticeable free-surface effects on the flow field. In addition, stem reconfiguration further reduces the effective canopy height, increasing the distance from the free surface. Therefore, free-surface effects are expected to be negligible and are not explicitly resolved in the present simulations.

The flexibility of aquatic vegetation in nature typically ranges from $K = 2.0 \times 10^{-4}$ to $K = 3.0 \times 10^{2}$ (Luhar & Nepf 2011). Our previous study (Chen & Li 2025) showed that stems with $K > 1.0$ behave as rigid bodies; hence only cases with $K \leqslant 1.0$ are considered here. To systematically investigate the effect of flexibility on the flow and stem dynamics, a broad range of K is considered, with cases corresponding to $K = 1$, 0.32, 0.1, 0.032, 0.01 and 0.0032. The stem density is set to $\rho_s/\rho = 2$. The simulations were performed on the computational facilities of the National Supercomputing Centre, Singapore. The non-dimensional time step is set to 2×10^{-5}, yielding a CFL number of approximately 10^{-3}. Each case was computed in parallel using 256 CPU cores, and required approximately 3–4 months of wall-clock time per case.

3. Results

This section presents the stem-array dynamics, stem deformation, vortex dynamics, inter-stem interactions, flow distributions, hydrodynamic loading and bed shear stress as functions of stem flexibility. Table 1 summarises the key parameters of the investigated cases. Three distinct response regimes are identified within the simulated range of K. For brevity, only the representative cases $K = 1$, 0.32, 0.1 and 0.032 are presented, as they capture all three response regimes.

3.1. *Dynamics of the flexible stem array*

The dynamics of the stem array is crucial for understanding inter-stem interactions and the resulting flow redistribution within and above the canopy. Figures 2 and 3 present instantaneous snapshots of the array dynamics at different flexibility values (K) from

https://doi.org/10.1017/jfm.2026.12218 Published online by Cambridge University Press

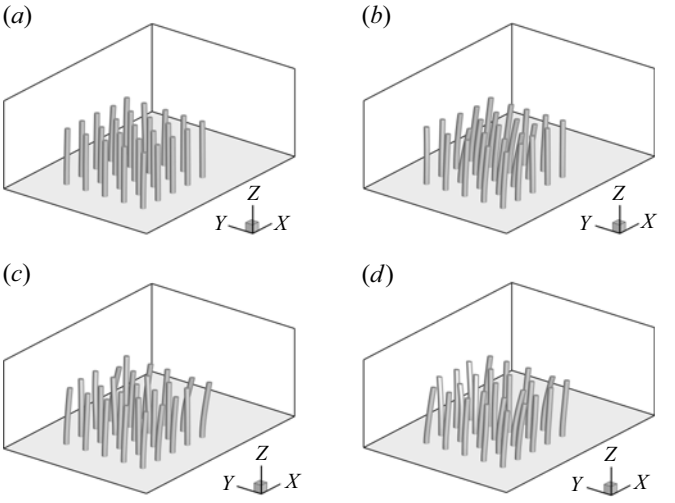


Figure 2. Instantaneous dynamics of the flexible stem array for different flexibilities (K), viewed from the side, with (a) $K = 1$, (b) $K = 0.32$, (c) $K = 0.1$ and (d) $K = 0.032$. The top-view visualisations highlight the spatial deformation patterns and collective motions of the stems across varying K. Flow structures are omitted for clarity.

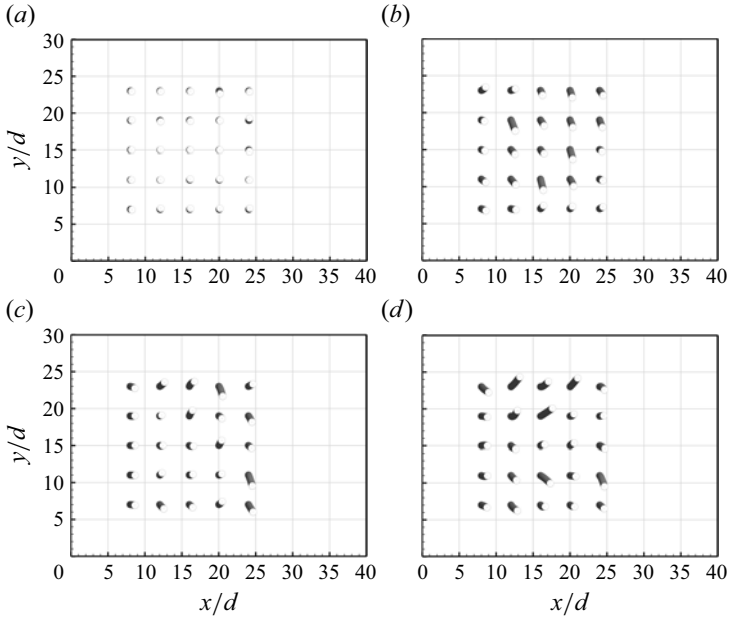


Figure 3. Instantaneous dynamics of the flexible stem array for different flexibilities (K), viewed from above, with (a) $K = 1$, (b) $K = 0.32$, (c) $K = 0.1$ and (d) $K = 0.032$. The top-view visualisations highlight the spatial deformation patterns and collective motions of the stems across varying K. Flow structures are omitted for clarity.

side and top views, respectively. Distinct dynamic regimes emerge as K decreases. At $K = 1$, the stems behave almost rigidly, exhibiting negligible deformation and oscillations; see figure 2(a). From the top view (figure 3a), only minor motion is observed for the downstream stems, confirming the quasi-rigid response of the array. When $K = 0.32$, stem

https://doi.org/10.1017/jfm.2026.12218 Published online by Cambridge University Press

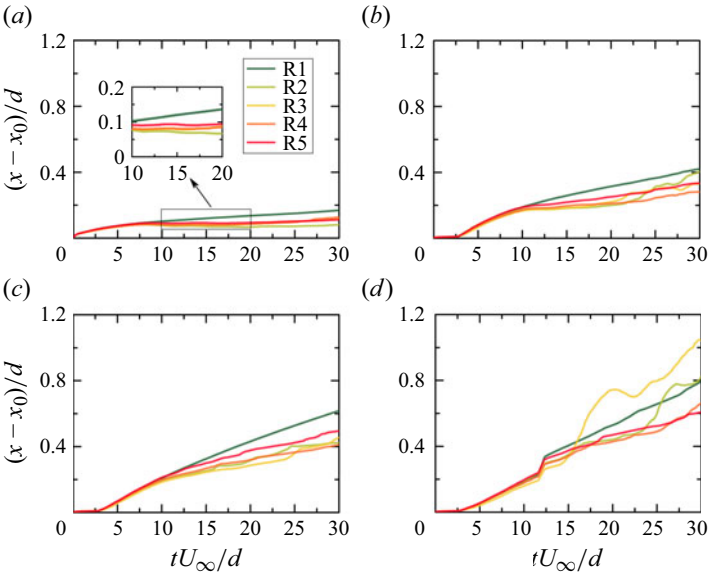


Figure 4. Time evolution of the streamwise tip displacement for stems in different rows, with (*a*) $K = 1$, (*b*) $K = 0.32$, (*c*) $K = 0.1$ and (*d*) $K = 0.032$. For each case, the displacements are ensemble-averaged over all stems within a row.

deformation becomes more pronounced, as shown in figure 2(*b*). As will be shown later, the stem oscillation at this K is significantly stronger than at other K values. The top view (figure 3*b*) reveals coherent motion across the array, particularly in the downstream rows, where the stems experience stronger fluctuating forces despite the first-row stems directly facing the freestream. At $K = 0.1$, the array exhibits patterns similar to those at $K = 0.32$, with mild deformation in the first row, and increasingly stronger oscillations downstream, corresponding to intensified vortex activity, as shown in figure 2(*c*). The deformation and oscillation amplify towards the array's trailing edge; see figure 3(*c*).

As K further decreases, deformation becomes more significant and extends across the entire array. For $K \leqslant 0.032$, the first-row stems undergo substantial deformation, indicating that under high flexibility, the leading stems experience significant flow-induced bending, analogous to the lodging state commonly observed in natural aquatic vegetation (Chen & Li 2025). As shown in figure 2(*d*), downstream stems exhibit greater deflection and increasingly complex motions, including higher-order modal dynamics. With weaker structural resistance, stems undergo more pronounced deformation and more irregular motion patterns. Consequently, the flow within and above the array becomes highly heterogeneous. The top-view visualisations (figure 3*d*) further confirm extensive deformation across both front and downstream rows, with notably displaced freestream-side stems. These behaviours correspond to intensified vortex interactions and reduced inter-stem shielding, as discussed later.

3.2. *Evolution of stem displacements*

In this subsection, we examine the temporal evolution of stem displacements in three spatial directions, with particular focus on the streamwise motion of stem tips across the five rows of the array. Figure 4 shows the trajectories of the stem tips over non-dimensional time. The results show that the streamwise displacements increase progressively downstream, and are strongly dependent on the flexibility parameter K.

https://doi.org/10.1017/jfm.2026.12218 Published online by Cambridge University Press

As K decreases, the stem tips exhibit larger streamwise excursions from their initial positions, reflecting enhanced structural compliance and hydrodynamic forcing.

With $K = 1$, the stems behave almost rigidly, and the maximum non-dimensional streamwise displacement remains below 0.2. As shown in figure 4(a), the streamwise displacement initially decreases from the first to the second row, and then increases downstream, reaching a secondary maximum near the fourth row. The reduced displacement in the second row results from the shielding effect of the upstream row, which directly faces the incoming flow and induces a substantial momentum deficit in the downstream region. Consequently, the second-row stems experience a diminished drag force and weaker flow excitation. Further downstream, developing vortical structures gradually reenergise the flow, leading to larger displacements. The smaller displacement observed in the last row indicates that for a relatively rigid array, the front row provides the dominant damping on the incoming current.

With $K = 0.32$, a similar trend is observed, though the overall deformation amplitude increases. As shown in figure 4(b), the first-row stems undergo the largest deflection, indicating strong interaction with the freestream and the most effective flow attenuation. The minimum displacement occurs at the fourth row, shifted further downstream compared with the $K = 1$ case. Notably, oscillatory behaviour emerges in the second and third rows, suggesting enhanced unsteady hydrodynamic coupling among the stems.

When K is further reduced to 0.1, the streamwise displacement grows markedly, reaching approximately 0.6 in the first row; see figure 4(c). The pattern of decay and recovery with increasing row number persists, though the oscillations become more pronounced. The lowest displacement is observed in the fourth row, while the streamwise displacements are comparable for the middle three rows. However, with $K = 0.032$, a transition occurs: the mid-array stems (R2 and R3) exhibit comparable displacements to those of the first-row stems (see figure 4d), implying that local drag and flow acceleration within the array govern the deformation more strongly than direct flow exposure.

Across all simulated cases, the results demonstrate that the damping role of successive rows increases once the internal flow develops sufficiently within and above the canopy. This progressive modulation of stem response by flexibility and row position provides key physical insights into momentum absorption, and has important implications for optimising vegetation-based coastal protection and wave attenuation designs.

The temporal evolution of the vertical displacements of stem tips in each row is presented in figure 5. With $K = 1$, the vertical displacements are negligible (figure 5a), consistent with the small streamwise excursions reported earlier, and confirming the minimal deformation of the relatively rigid arrays. As K decreases, the stems bend progressively downwards, and the vertical displacements become more pronounced (figures 5b–d). With $K = 0.32$, the downward deflection exceeds that with $K = 0.1$, despite the latter being more flexible. This counterintuitive behaviour indicates that the stems exhibiting stronger dynamic responses undergo larger instantaneous deformation. With $K = 0.032$, substantial vertical displacements develop, particularly in the middle rows of the array. This pattern mirrors the streamwise deflection shown in figure 4(d), suggesting that flow acceleration within the array enhances stem bending and reconfiguration. The close correspondence between the vertical and streamwise motions highlights the nonlinear coupling among flexibility, local hydrodynamics and inter-stem interactions, which governs the redistribution of momentum and turbulence within the canopy.

The transverse motion of stem tips is examined next, as vortex-induced vibration (VIV) of flexible stems develops primarily in the cross-flow direction. Figure 6 shows the temporal evolution of transverse tip displacement for arrays with different flexibilities.

https://doi.org/10.1017/jfm.2026.12218 Published online by Cambridge University Press

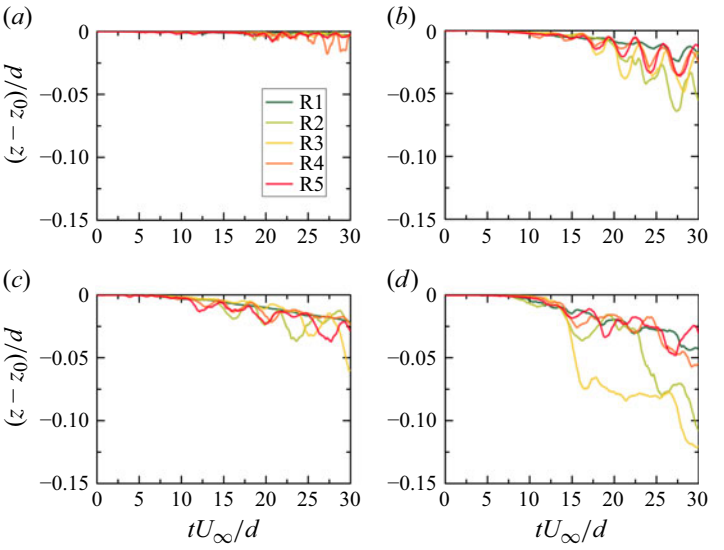


Figure 5. Time evolution of the vertical tip displacement for stems in different rows, with (*a*) $K = 1$, (*b*) $K = 0.32$, (*c*) $K = 0.1$ and (*d*) $K = 0.032$. The values represent the row-averaged vertical motion of the stem tips.

With $K = 1$, the stems remain nearly stationary initially, with oscillations developing at approximately $tU_\infty/d = 15$. The response is weak in the first column (C1, figure 6*ai*), and becomes even smaller towards the array centre (C2 and C3, figures 6*a*ii,*a*iii). In contrast, likely due to reduced downstream confinement and more developed vortex shedding, the stems in the last row exhibit the largest oscillation amplitudes. In the outer columns (C4 and C5), oscillations develop with larger initial amplitudes and slight phase differences (figures 6*a*iv,*a*v), implying an early breakdown of flow symmetry.

With $K = 0.32$, oscillations develop earlier, and their amplitudes increase markedly. The stems oscillate more synchronously, with larger displacements and well-defined phase relationships, indicating near lock-in between vortex shedding and structural frequency (figures 6*bi–bv*). The largest oscillations occur in the outer columns (C1 and C5), whereas the stems in the central region oscillate nearly in phase, highlighting the influence of organised wake structures on array dynamics.

With $K \leqslant 0.1$, the oscillations become highly irregular, with smaller and more scattered amplitudes (figures 6*c*,*d*). Motion initiates earlier in the outer columns, whereas the leading stems remain nearly stationary because of strong flow blockage (figures 6*c*i,*c*v). Downstream stems, exposed to less shielding, exhibit more pronounced oscillations, consistent with less constrained vortex shedding and reduced hydrodynamic coupling between rows. Several downstream stems also display pronounced one-sided deflection (figures 6*d*ii,*d*iv), suggesting that strong inter-stem interactions and local flow disturbances disrupt the global coherence of the oscillation response.

3.3. *Vortex dynamics and inter-stem interactions*

Understanding the evolution of vortex dynamics and inter-stem interactions is essential for elucidating the coupling between flow structures and stem responses. Figure 7 shows instantaneous 3-D vortical structures of flexible stem array with different flexibilities, viewed from the top. Distinct flow regimes emerge as K decreases, highlighting the modulation of wake dynamics by structural flexibility.

https://doi.org/10.1017/jfm.2026.12218 Published online by Cambridge University Press

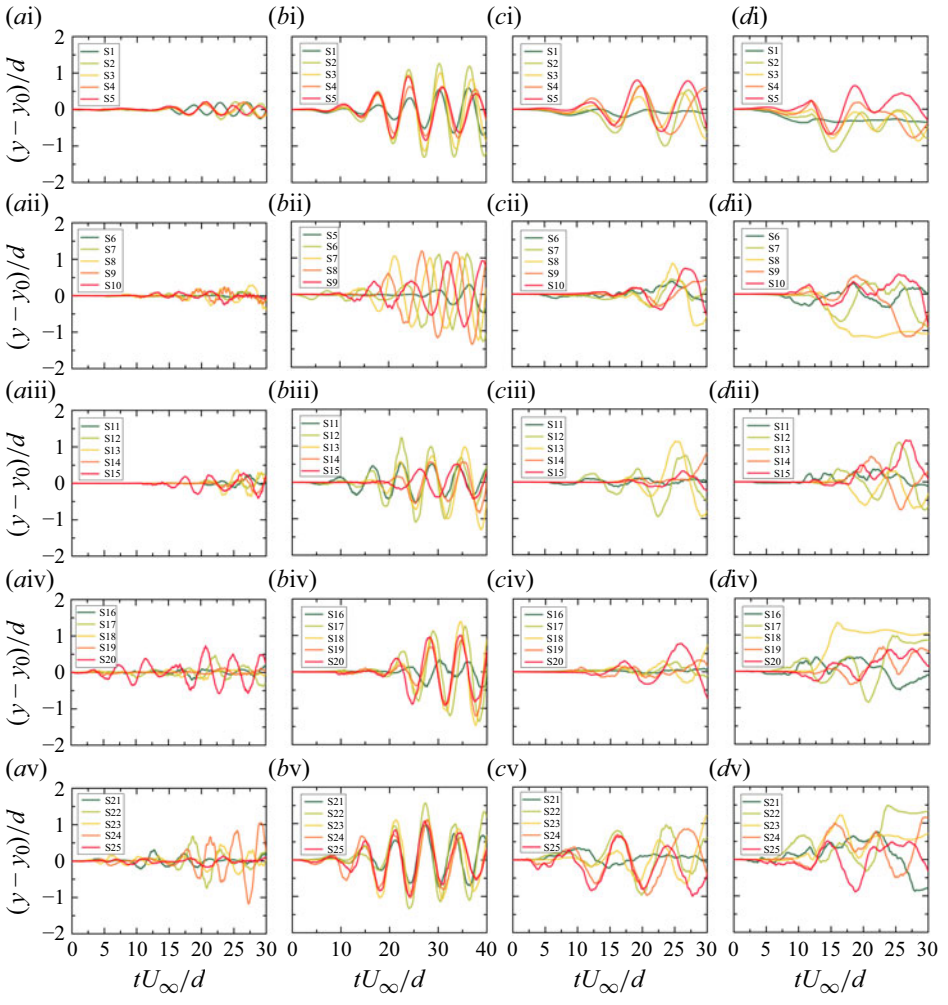


Figure 6. Time evolution of the transverse tip displacement of the stem array with (*a*) $K = 1$, (*b*) $K = 0.32$, (*c*) $K = 0.1$ and (*d*) $K = 0.032$. Here, S*i* denotes the stem numbered i, as indicated in figure 1.

With $K = 1$, the stems behave nearly rigidly, and the flow field closely resembles that of a rigid array. Vortex shedding initiates at the trailing edge of the first row, with these vortices impinging directly on downstream stems. The separated vortices from subsequent rows are smaller and gradually transform into streamwise vortices. The top view (figure 7*a*) reveals a tandem bi-vortex-street pattern (Sumner 2010), with evident lateral interference between adjacent columns. The wake is asymmetric, i.e. narrower on the inner side and broader on the freestream side, reflecting stronger outer vortices and confinement effects (Chang *et al.* 2017). The strongest vortices appear around the third row, after which they dissipate downstream.

With $K = 0.32$, the stem response reaches its maximum, and the vortex system becomes considerably more energetic. Alternate vortex shedding occurs from the front-row stems, but due to stem deformation, the vortices shed from the tips are phase-lagged relative to those from the lower portions. The top view (figure 7*b*) shows approximately in-phase shedding among the five front stems, followed by strong interactions with newly formed downstream vortices. Beyond the second row, the wake becomes increasingly

https://doi.org/10.1017/jfm.2026.12218 Published online by Cambridge University Press

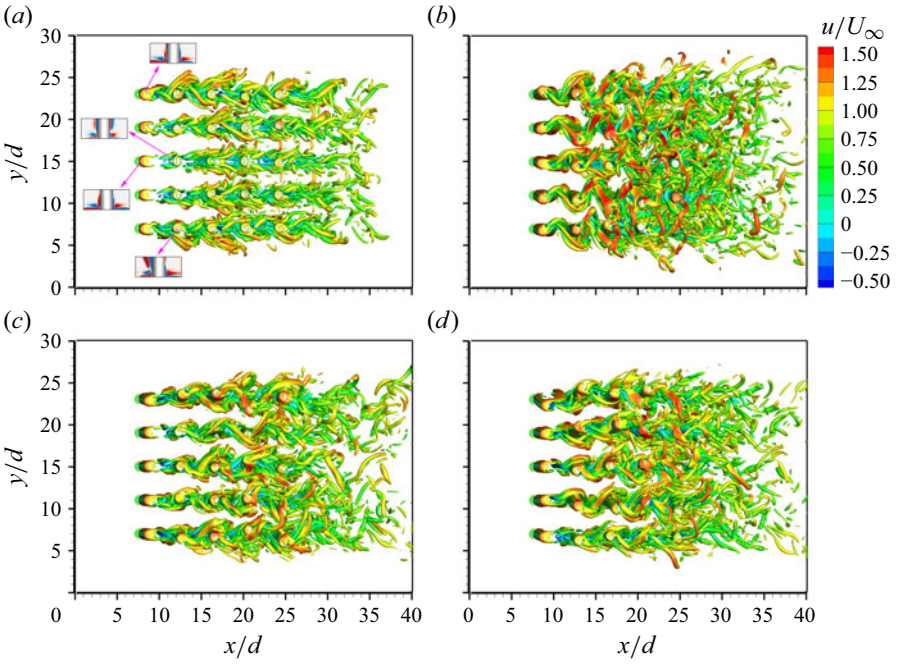


Figure 7. Instantaneous 3-D vortex dynamics of the flexible stem array, with (*a*) $K = 1$, (*b*) $K = 0.32$, (*c*) $K = 0.1$ and (*d*) $K = 0.032$. Vortical structures are visualised using the Q-criterion ($Q = 2.5$; Hunt *et al.* 1988). Insets of the horseshoe vortex system visualised by the x-vorticity are provided in (*a*). Here, $\omega_x^* \equiv (d/U_\infty)(\partial w/\partial y - \partial v/\partial z)$.

irregular, and finer vortices fill the inter-column gaps, producing a substantial reduction in streamwise velocity within the array. Above the canopy, the vortices dissipate gradually, without forming large-scale coherent rollers.

With $K = 0.1$, the overall vortex intensity weakens slightly. Vortex shedding from the leading stems persists but becomes less organised, with smaller-scale eddies convected downstream. The top view (figure 7*c*) shows more irregularity, particularly near the wake of the downstream rows, where direct vortex-stem interactions remain visible. This pattern is reminiscent of the $K = 1$ case, indicating a partial recovery of rigid-like behaviour.

With $K \leqslant 0.032$, stem deformation is more pronounced, causing out-of-phase shedding and column-dependent differences in wake topology. As shown in figure 7(*d*), vortices from the first two rows form narrow wakes, leaving wider gaps for throughflow. Downstream, however, the flow becomes dominated by finer, disordered vortices that occupy the inter-stem spaces. Chaotic motion and asymmetric flow organisation are observed in these large-deformation cases.

The overall patterns of 3-D vortical structures around individual stems are qualitatively similar across all cases, yet discernible differences arise owing to the hydrodynamic interferences among neighbouring stems. Horseshoe vortices consistently develop upstream of the leading-row stems, and to a lesser extent around some downstream stems; see the insets in figure 7(*a*). Their strength is, however, noticeably weaker than that observed for a single flexible stem with the same K (Chang *et al.* 2017; Chang *et al.* 2020). This attenuation results from the combined effects of upstream blockage and downstream sheltering within the array; see figures 10 and 13 below.

The influence of stem flexibility on the formation of the horseshoe vortex is also evident. With $K = 1$, the stems undergo smaller oscillations, which tend to suppress the near-wall

https://doi.org/10.1017/jfm.2026.12218 Published online by Cambridge University Press

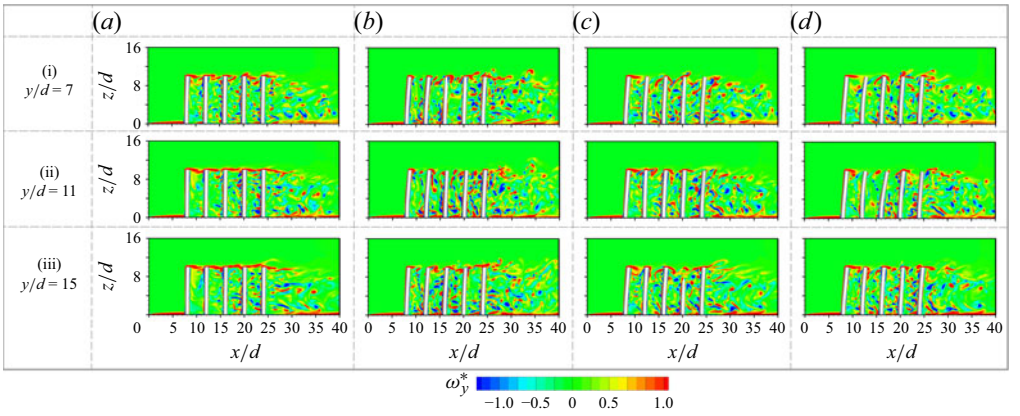


Figure 8. Instantaneous y-vorticity fields around and downstream of the flexible stem array at various transverse positions, with (*a*) $K = 1$, (*b*) $K = 0.32$, (*c*) $K = 0.1$ and (*d*) $K = 0.032$. The corresponding plane locations are indicated in figure 1. Here, $\omega_y^* \equiv (d/U_\infty)(\partial u/\partial z - \partial w/\partial x)$.

flow separation, and consequently weaken the horseshoe vortex. A similar modulation of the vortex system by stem motion has been reported in the single-stem configuration (Chen & Li 2025).

In addition to the horseshoe vortex, distinct free-end vortices develop near the stem tips, as revealed by the y-vorticity distribution in figure 8. These vortices detach into the wake and interact directly with downstream stems. Advected by the upward flow, they convect downstream without approaching the bed. Their subsequent evolution is strongly influenced by the stem dynamics. With $K = 1$, where stem deformation and oscillation amplitudes are small, the free-end vortices tend to reattach near the tips of the downstream stems (figure 8*a*). As K decreases, the free-end vortices propagate through the inter-stem gaps and undergo increasingly complex interactions, which are strongly modulated by the transverse stem motions (figures 8*b–d*).

A relatively weak base vortex is also observed behind the trailing stems, corresponding to the lower local velocity induced by the shielding effect. Likewise, the shear layers enveloping the stems are considerably weakened, forming elongated spanwise vortices. The attenuated intensity of these structures reflects the reduced mean velocity within the array. The spanwise vortices play a key role in mediating the exchange of mass and momentum between the canopy and the overlying flow. These spanwise vortices, generated by shear layers at the canopy top, are further modulated by the penetration of outer-layer streamwise vortices. In the wake region, the streamwise vortices emerge from the stretching of spanwise rollers, and subsequently interact with the downstream stems due to the short inter-stem spacing. Furthermore, similar to the single-stem configuration, the hairpin-like vortices are observed in the wake.

The three-dimensionality and intensity of the wake can be quantified through enstrophy, which characterises the spatial distribution of vorticity magnitude (Papaioannou *et al.* 2006; Thapa *et al.* 2014). Here, we examine the enstrophy to evaluate how stem flexibility modulates rotational motions within the flow. The enstrophies associated with different components are defined as

$$\varepsilon_x = \int_V \omega_x^2 \,\mathrm{d}V,\ \varepsilon_y = \int_V \omega_y^2 \,\mathrm{d}V,\ \varepsilon_{x+y} = \int_V (\omega_x^2 + \omega_y^2) \,\mathrm{d}V,\ \varepsilon_z = \int_V \omega_z^2 \,\mathrm{d}V, \tag{3.1}$$

where V denotes the volume of the computational domain.

https://doi.org/10.1017/jfm.2026.12218 Published online by Cambridge University Press

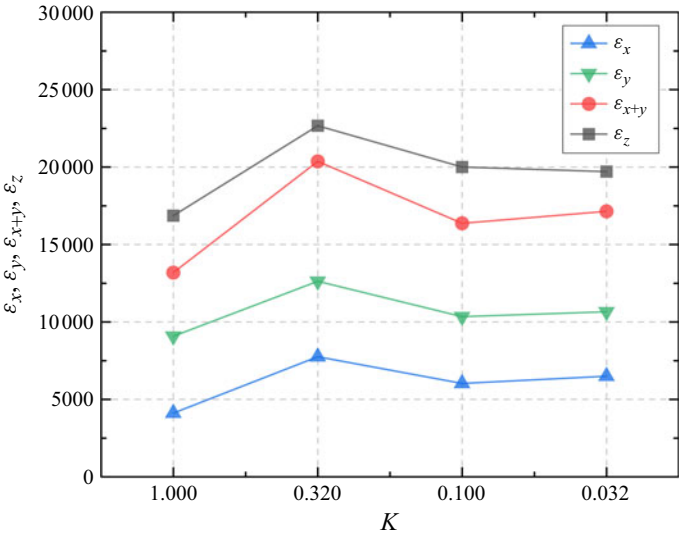


Figure 9. Statistics of the vorticity components within the computational domain for flow through flexible stem arrays. The enstrophies associated with different rotational components are compared to illustrate how stem flexibility modulates wake three-dimensionality.

Figure 9 shows the variation of the enstrophy components with stem flexibility. As K decreases, all components exhibit the same non-monotonic trend, increasing to a maximum before decreasing. This behaviour is consistent with the coupling between stem motion and vortical activity, whereby stronger FSI produces larger oscillation amplitudes and more intense vortex dynamics. All enstrophy components reach their maximum at $K = 0.32$, corresponding to the strongest stem oscillation. These results indicate that intermediate flexibility promotes the most vigorous 3-D vortex dynamics within the canopy, and consequently the greatest potential for wave-energy dissipation.

The vertical variation of vortex dynamics provides important insights into the distributions of bed shear stress, turbulence generation and momentum transport within and above the stem array. Figure 10 shows the instantaneous z-vorticity fields at representative elevations for different flexibility cases. Near the bed ($z/d = 0.1$), where the impermeable wall constrains vertical motion, the vortex shedding pattern varies markedly with K. With $K = 1$, distinct vortex shedding occurs from the leading-row stems, but weakens progressively downstream (figure 10*ai*), reflecting the reduction in local flow momentum caused by the blockage from the nearly rigid stems. As K decreases, stem motion at higher elevation exerts a stronger influence on the near-wall flow (figures 10*b*i,*c*i,*d*i). Consequently, vortex shedding behind the stem weakens, whereas vortical activity farther downstream is enhanced, particularly for $K = 0.32$, where vigorous oscillation promotes strong local unsteadiness. This modulation of near-wall vortical activity indicates that flexibility modifies both bed shear stress and turbulence generation, the two primary processes governing sediment entrainment (Zhao & Nepf 2021).

At the mid-canopy elevation ($z/d = 5.0$), wall effects become negligible, and the flow is governed by FSI. With $K = 1$, two distinct shedding regimes emerge (figure 10*a*ii): the freestream-side columns generate strong, detached vortices that convect downstream, whereas vortex shedding within the inner columns is suppressed by wake interference,

https://doi.org/10.1017/jfm.2026.12218 Published online by Cambridge University Press

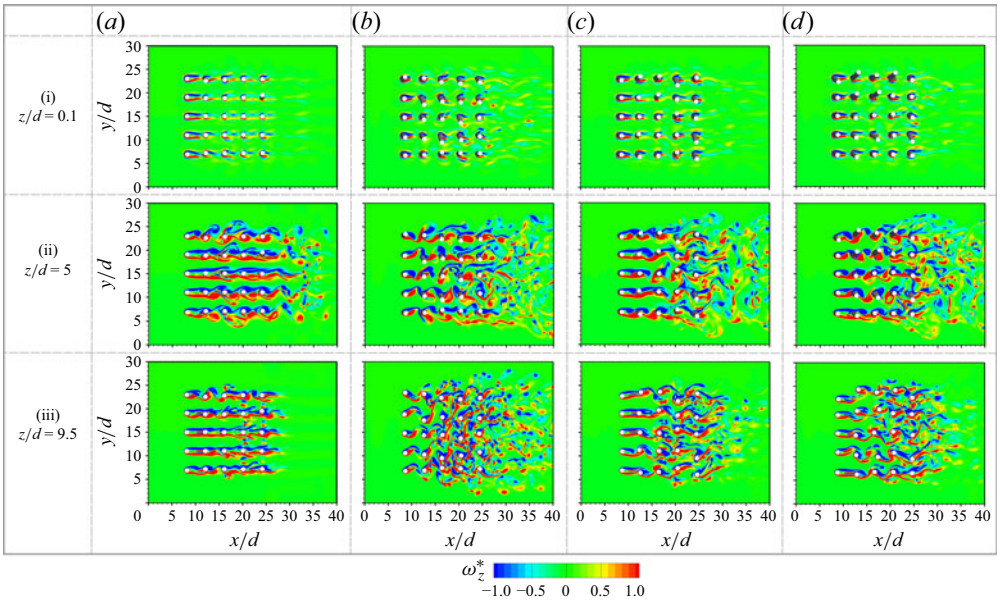


Figure 10. Instantaneous z-vorticity fields at different vertical planes for flow through flexible stem arrays, with (*a*) $K = 1$, (*b*) $K = 0.32$, (*c*) $K = 0.1$ and (*d*) $K = 0.032$. Here, $\omega_z^* \equiv (d/U_\infty)(\partial u/\partial x - \partial v/\partial y)$.

producing elongated shear layers that reattach to the downstream stems. Such shear-layer reattachment inhibits stem oscillation, and stabilises the local flow. In contrast, with $K = 0.32$, pronounced alternating vortices develop within the gaps, and impinge directly on downstream stems (figure 10*bii*), leading to larger oscillation amplitudes and enhanced lateral mixing. The more flexible cases ($K = 0.1$ and 0.032) exhibit mixed behaviour: shear-layer reattachment dominates in the upstream rows, whereas vortex–stem interactions become increasingly important downstream (figures 10*c*ii,*d*ii), indicating a gradual transition in the interaction regime with increasing flexibility.

In the upper canopy region ($z/d = 9.5$), free-end effects and stem reconfiguration dominate the vortex dynamics. With $K = 1$, vortex shedding weakens progressively towards the stem tips (figure 10*a*iii). The inner columns remain dominated by shear-layer reattachment, whereas outer stems continue to shed isolated vortices that induce asymmetric oscillations. With $K = 0.32$, coherent vortices persist throughout the upper canopy, and penetrate farther downstream (figure 10*b*iii), suggesting enhanced momentum transfer and turbulence generation. In contrast, for the highly flexible cases ($K = 0.1$ and 0.032), large stem deflections substantially distort the wake topology. Vortices shed from the upstream stems impinge directly on downstream stems (figures 10*c*iii,*d*iii), but their strength decreases towards the free ends because flow separation is progressively reduced. Overall, increasing flexibility weakens large-scale vortex coherence while enhancing local turbulent mixing, leading to increasingly anisotropic turbulence and enhanced energy dissipation within the canopy wake.

3.4. *Velocity distribution*

The spatial distribution of the streamwise velocity provides key insights into how stem flexibility modifies flow resistance, momentum transport and sediment dynamics within vegetation canopies (Wang *et al.* 2022*b*). Figure 11 shows the instantaneous streamwise velocity fields at representative transverse planes for cases $K = 1$, 0.32, 0.1 and 0.032.

https://doi.org/10.1017/jfm.2026.12218 Published online by Cambridge University Press

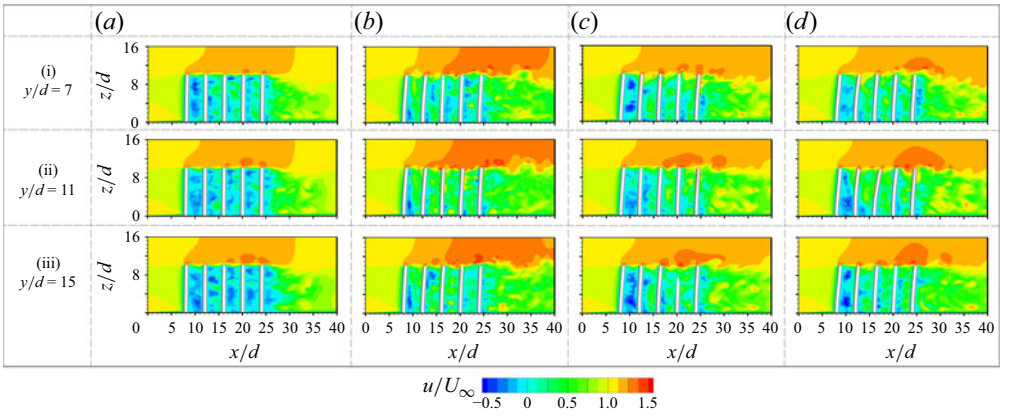


Figure 11. Instantaneous streamwise velocity fields around and downstream of the flexible stem array at various transverse positions, with (*a*) $K = 1$, (*b*) $K = 0.32$, (*c*) $K = 0.1$ and (*d*) $K = 0.032$. The corresponding plane locations are indicated in figure 1.

For the relatively rigid case ($K = 1$), the stems undergo little deformation, and the flow closely resembles that through a rigid array. At $y/d = 7$, the incoming flow is strongly decelerated by the leading-row stems (figure 11*a*i). Immediately downstream of each stem, recirculation regions ($u < 0$) develop due to shear-layer reattachment and periodic vortex shedding. The flow within the array remains at a low velocity, while the flow above the array is accelerated relative to inflow (Nepf 2012; Tschisgale *et al.* 2021), reflecting momentum redistribution over the vegetated roughness layer. Downstream of the array, the streamwise velocity gradually recovers, forming alternating low- and high-speed streaks associated with the stem-generated shear layers.

As K decreases, stem reconfiguration progressively alters the wake topology. With $K = 0.32$, pronounced stem deformation and oscillation contract the recirculation regions and enhanced local mixing (figure 11*b*i; Wang *et al.* 2022*a*,*b*). The reduced frontal blockage accelerates the flow through the inter-stem gaps, while the reverse-flow regions behind individual stems are substantially weakened. In contrast, for the more flexible cases ($K = 0.1$ and 0.032), the less synchronised stem motion produces irregular flow acceleration between adjacent rows, and a more heterogeneous velocity field within the array (figures 11*c*i,*d*i). Consequently, the velocity above the canopy is slightly lower than that for $K = 0.32$.

At $y/d = 11$ and 15, the streamwise velocity deficit behind the stems becomes more pronounced for $K = 1$, 0.1 and 0.032 (figures 11*a*ii,*a*iii,*c*ii,*c*iii,*d*ii,*d*iii), indicating stronger blockage and greater momentum loss within the interior of the array. In contrast, with $K = 0.32$, vigorous stem oscillation alleviates the velocity deficit (figures 11*b*ii,*b*iii), maintaining a more uniform velocity distribution throughout the canopy.

Within the gaps between adjacent columns, the streamwise velocity locally exceeds the incoming velocity, forming high-momentum corridors that gradually weaken towards the canopy exit (not shown).

The influence of stem flexibility on the streamwise velocity field is shown in figure 12. Along the first stem row, the streamwise velocity locally exceeds the inflow value, forming narrow jet-like streams (figures 12*a*–*d*, row *i*). Near the stem tips, however, the flow is increasingly governed by stem motion, reflecting the combined effects of flow separation and deformation-induced blockage, which are most pronounced for the most flexible case ($K = 0.032$). Downstream, the wakes of the upstream stems strongly modify the

https://doi.org/10.1017/jfm.2026.12218 Published online by Cambridge University Press

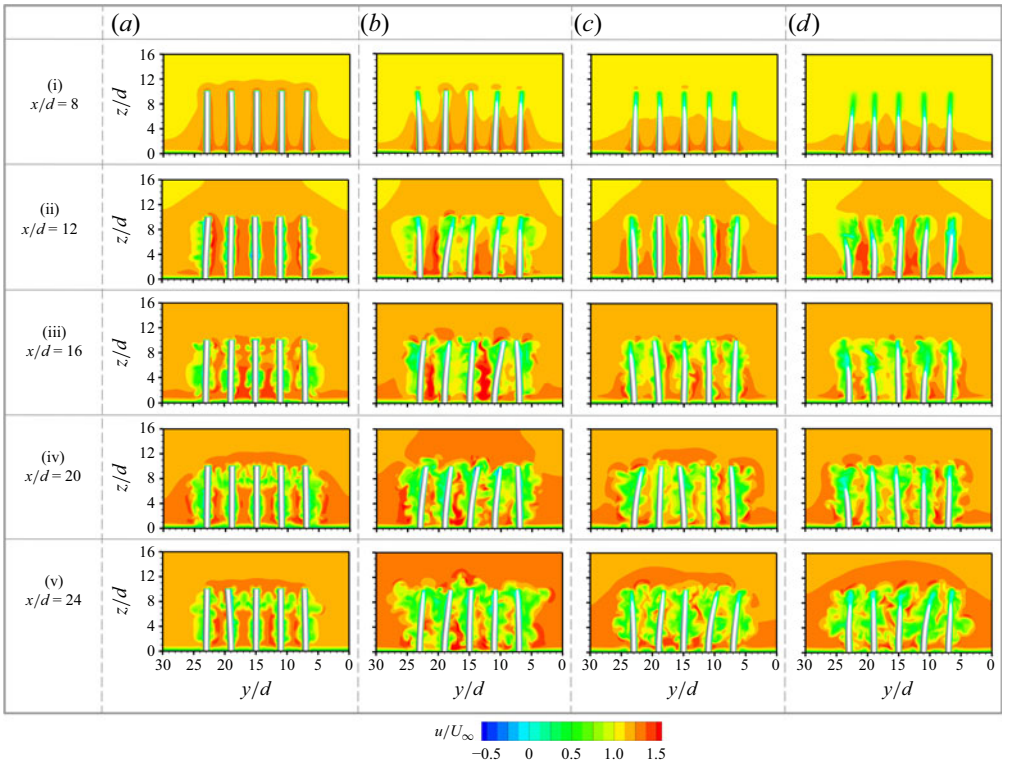


Figure 12. Instantaneous streamwise velocity fields around and downstream of the flexible stem array at various streamwise positions, with (*a*) $K = 1$, (*b*) $K = 0.32$, (*c*) $K = 0.1$ and (*d*) $K = 0.032$. The corresponding plane locations are indicated in figure 1.

local flow, producing alternating high- and low-velocity streaks between successive rows (figures 12*a*–*d*, rows *ii*–*v*). Their spatial distribution varies markedly with K, owing to the combined effects of stem deformation and oscillation.

Within the inter-row gaps, the flow is clearly partitioned into low- and high-momentum regions (not shown). Low-momentum zones develop in the stem wake, whereas the high-momentum flow is confined to the inter-stem gaps. Their size and persistence depend strongly on the stem dynamics. For $K = 0.32$, pronounced stem oscillations broaden the wake regions and increase their temporal variability, whereas they remain relatively narrow and steady in the nearly rigid case. Farther downstream, the influence of stem motion becomes increasingly pronounced, promoting the wake expansion, and enhancing the spatial heterogeneity of the velocity field. The associated momentum redistribution also contributes to localised high-momentum flow along the outer edge of the array.

The distribution of streamwise velocity at different elevations provides crucial insights into the vertical structure of momentum transport, which directly influences sediment entrainment, near-bed shear stress, and the spatial distribution of TKE. Figure 13 shows the instantaneous streamwise velocity fields, superimposed with streamlines, at representative vertical planes for $K = 1$, 0.32, 0.1 and 0.032.

Near the impermeable bed ($z/d = 0.1$), the streamwise velocity remains small throughout the domain owing to the no-slip boundary condition (figures 13(*a*–*d*, row *i*). The weak shear layers at this elevation correspond to a relatively low local Re, leading to limited turbulence production. Nevertheless, small-scale velocity fluctuations persist

https://doi.org/10.1017/jfm.2026.12218 Published online by Cambridge University Press

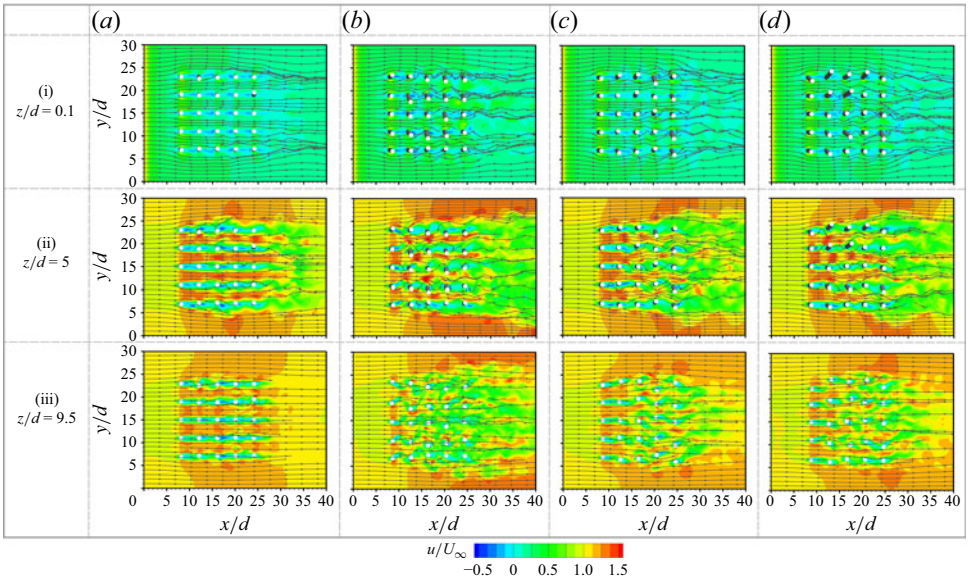


Figure 13. Instantaneous streamwise velocity fields around and downstream of the flexible stem array at different vertical elevations, with (*a*) $K = 1$, (*b*) $K = 0.32$, (*c*) $K = 0.1$ and (*d*) $K = 0.032$. Streamlines are superimposed as solid lines in each plot.

within the array, particularly for $K = 0.32$, 0.1 and 0.032, suggesting that stem motion still induces local flow disturbances and weak secondary motions despite strong viscous damping.

At the mid-canopy elevation ($z/d = 5.0$), the overall flow pattern is similar across all cases (figures 13*a–d*, row *ii*). The streamwise velocity reaches its maximum within the inter-column gaps and along the canopy edges, where bypass flow dominates. The internal structure of these high-speed corridors, however, depends strongly on stem flexibility. For $K = 0.32$, vigorous stem oscillations periodically constrict the jet-like flow, narrowing the high-speed corridors and enhancing the local shear (figure 13*b*ii). By contrast, the remaining cases ($K = 1$, 0.1 and 0.032) exhibit weaker velocity modulation (figures 13*a*ii,*c*ii,*d*ii), consistent with their less pronounced stem oscillation.

Near the free ends ($z/d = 9.5$), the flow becomes increasingly influenced by stem motion and vertical momentum exchange. For $K = 1$, the streamwise velocity within the inter-column gaps increases with height (figure 13*a*iii), reflecting flow acceleration above the canopy and the downward entrainment of high-momentum fluid. In contrast, for $K = 0.32$, strong oscillations near the stem tips reduce the mean velocity within the array, producing elongated low-velocity regions (figure 13*b*iii). For $K = 0.1$ and 0.032, the velocity distribution shows intermediate characteristics, i.e. localised acceleration within the gaps, and persistent low-speed wakes behind the stems. Meanwhile, the downstream velocity recovers more rapidly with increasing height, indicating enhanced momentum exchange with the overlying flow, and the gradual transition from the canopy flow to the outer boundary layer.

3.5. *Hydrodynamic drag*

The influence of stem flexibility on flow damping is manifested through the hydrodynamic drag acting on the stems. The spatial distribution of the streamwise drag force within the array provides valuable insight into the FSI and the overall energy dissipation of vegetated

https://doi.org/10.1017/jfm.2026.12218 Published online by Cambridge University Press

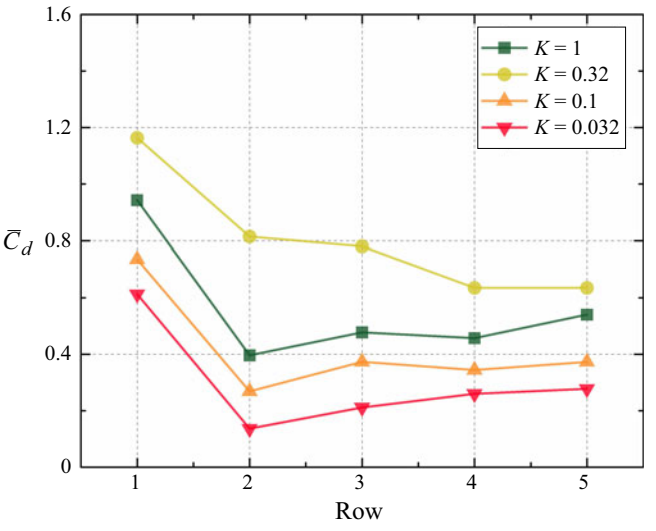


Figure 14. Distribution of the mean hydrodynamic drag on each row of stems, with $K = 1$, 0.32, 0.1 and 0.032. The drag coefficient for each row is obtained by averaging over five stems.

canopies. In this subsection, we present the time-averaged drag force on the stems for the four simulated cases.

Figure 14 presents the drag coefficient on the stems in each row for cases $K = 1$, 0.32, 0.1 and 0.032. Here, the drag coefficient of each row is defined as $C_d = (1/5)\sum C_{d,i} = (1/5)\sum F_{d,i}/0.5\rho U_\infty^2 dh$, where $F_{d,i}$ denotes the drag force of stem i. Across all simulated cases, the first row exhibits the largest drag coefficient. This indicates that, regardless of flexibility, the stems at the leading edge experience the strongest resistance to the incoming flow (Koken & Constantinescu 2021; Koken & Constantinescu 2023). This observation is physically reasonable, as the high-velocity incoming flow first impinges on these stems, producing a pronounced deceleration and near-zero velocity at their upstream surfaces.

Downstream of the first row, two distinct trends in the drag coefficient are observed. In case $K = 0.32$, the drag coefficient decreases monotonically with increasing row number, suggesting a progressive reduction in flow damping by successive rows. In contrast, for cases $K = 1$, 0.1 and 0.032, the drag coefficient attains its minimum at the second row, and subsequently increases gradually, albeit at a slower rate. The gradual increase is closely associated with the development of the gap flow between stems (Koken & Constantinescu 2021).

The variation in drag among the flexible stem arrays indicates that stems with moderate flexibility (case $K = 0.32$) exhibit the most effective damping. Figure 15 compares the dominant oscillation frequency, identified from the fast Fourier transform (FFT) of the spanwise velocity, with the natural frequency obtained from the FFT of the transverse tip displacement. The two frequencies coincide for case $K = 0.32$, indicating a lock-in state (Rosti *et al.* 2018; Rota *et al.* 2024). This finding is in agreement with our previous work (Chen & Li 2025), which demonstrated that a single flexible stem exhibits its largest oscillation amplitude under lock-in conditions. For both stiffer and more compliant stems (i.e. higher or lower K), this frequency matching is not achieved, leading to weaker stem responses and reduced flow damping. These results collectively elucidate the roles of flexibility in modulating hydrodynamic drag and energy dissipation within

https://doi.org/10.1017/jfm.2026.12218 Published online by Cambridge University Press

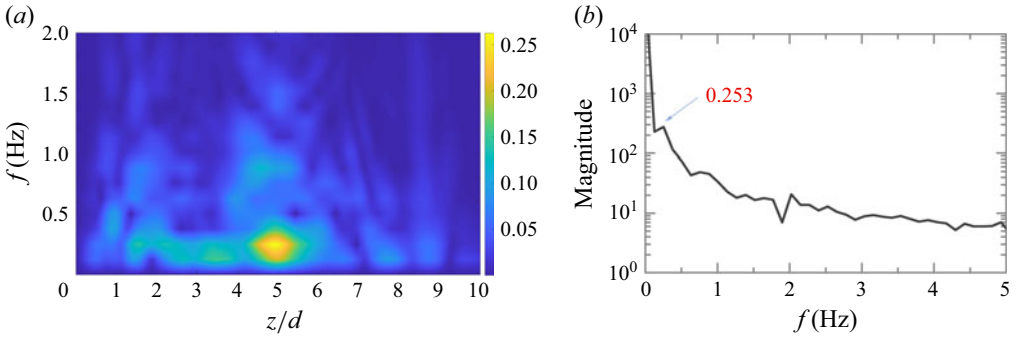


Figure 15. The FFT spectra of the spanwise velocity and the transverse tip displacement for case $K = 0.32$. The velocity is sampled at $x/d = 35$ and $y/d = 15$. The dominant oscillation frequency and the natural frequency are identified from the corresponding FFT spectra.

flexible vegetation arrays. Furthermore, the drag coefficients of stems within arrays are markedly lower than those of an isolated flexible element reported by Chen & Li (2025). This reduction largely arises from pronounced intra-array shielding, where the mutual sheltering among neighbouring stems attenuates the local velocity and momentum exchange, thereby diminishing the effective drag experienced by individual elements (Etminan *et al.* 2017).

3.6. *Bed shear stress*

The distributions of bed shear stress and TKE are fundamental for predicting sediment transport within vegetated arrays (Yang & Nepf 2018; Zhao & Nepf 2021). Gaining a mechanistic understanding of sediment transport within flexible arrays is helpful for advancing coastal protection and ecosystem resilience. Here, the bed shear stress and TKE are defined as $\tau_b = \rho u_\tau^2$ and $k = (\overline{u'^2} + \overline{v'^2} + \overline{w'^2})/2$, respectively, where u_τ is the local bed friction velocity, and u', v' and w' are the velocity fluctuations in the streamwise, transverse and vertical directions, respectively. Following Koken & Constantinescu (2021), u_τ is calculated using $u_\tau = (u_m \nu / n_1)^{1/2}$, where u_m is the velocity magnitude in a plane parallel to the bed situated at a distance n_1 from the wall. The first grid point above the wall is selected to estimate u_τ. As suggested by Chang *et al.* (2017) and Cheng *et al.* (2018), the sediment entrainment capacity of the flow depends on not only the mean near-bed friction velocity ($\bar{u}_\tau$) but also the r.m.s. value of the bed friction velocity (u_τ^{SD}), with the latter accounting for the influence of large-scale unsteadiness on the bed shear stress.

Figure 16 shows the mean bed shear stress distribution for cases $K = 1{-}0.032$. Overall, both the instantaneous and mean fields exhibit broadly similar spatial patterns across the different flexibility conditions. In all cases, the largest shear stresses occur along the lateral sides of the first-row stems, consistent with previous observations (Chang *et al.* 2017; Chang *et al.* 2020). This indicates that, irrespective of whether the stems behave rigidly or flexibly, the strongest bed forcing is concentrated at the upstream edge of the array. Downstream of the first row, however, clear differences emerge that are closely tied to stem flexibility. At intermediate flexibility, where the stem oscillations are most pronounced, the mean bed shear stress is substantially amplified compared with the other cases. This suggests that sediment transport is highly sensitive to stem oscillation amplitude. In addition, a slight increase in bed shear stress is observed near the downstream outlet, attributable to the recovery of the mean streamwise velocity, as is also evident in figures 7, 8 and 10.

https://doi.org/10.1017/jfm.2026.12218 Published online by Cambridge University Press

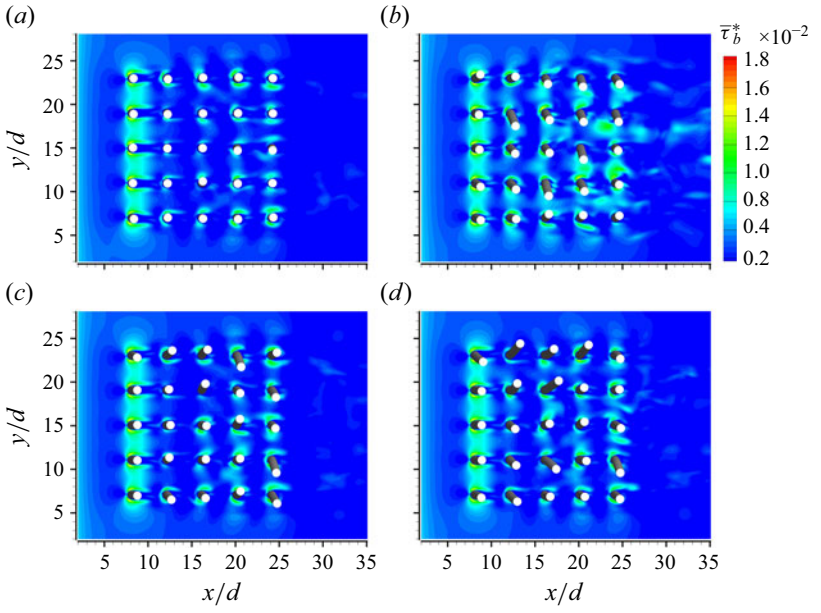


Figure 16. Time-averaged bed shear stress ($\overline{\tau}_b^*$) at the first grid above the bed, for cases (*a*) $K = 1$, (*b*) $K = 0.32$, (*c*) $K = 0.1$ and (*d*) $K = 0.032$. The averaging window is not sufficiently long; some instantaneous features remain visible.

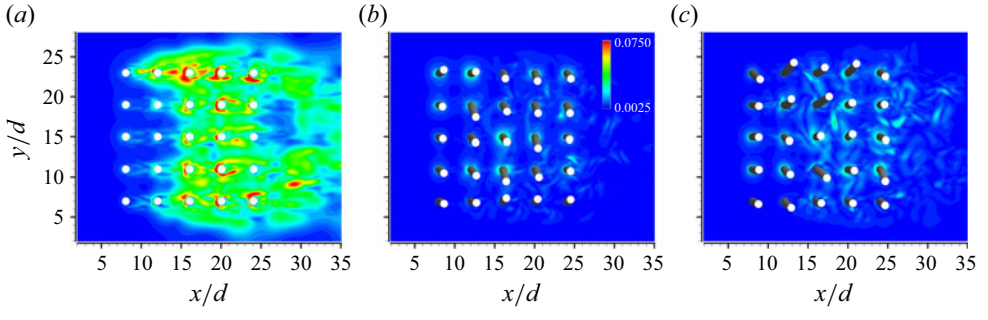


Figure 17. Distribution of the r.m.s. bed shear friction velocity at the first grid above the bed for (*a*) $K = 1$, (*b*) $K = 0.32$ and (*c*) $K = 0.032$.

Figure 17 shows the distributions of the r.m.s. bed friction velocity (u_τ^{SD}) at the first grid above the bed for cases $K = 1$, 0.32 and 0.032. In all three cases, elevated values of u_τ^{SD} occur downstream of the last two stem rows (figures 17*a–c*), corresponding to the formation and downstream evolution of wake vortices. The spatial distribution of u_τ^{SD} therefore reflects the coupling between stem motion and turbulence generation. As demonstrated in figures 12 and 13, stem oscillation redistributes TKE towards the upper canopy and the overlying flow, reducing the intensity of velocity fluctuations close to the bed. Consequently, u_τ^{SD} is significantly lower than in the nearly rigid case. This suggests that the enhanced unsteady motions are concentrated in the upper canopy, whereas turbulence penetration towards the bed is suppressed, leading to weaker bed shear fluctuations despite the intensified canopy-scale dynamics (Chen *et al.* 2026*c*).

https://doi.org/10.1017/jfm.2026.12218 Published online by Cambridge University Press

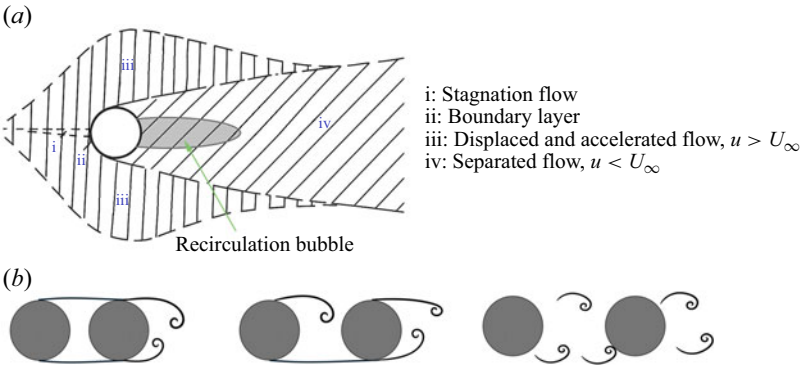


Figure 18. (*a*) Characteristic flow regions surrounding a circular cylinder, highlighting the separated shear layers and the near-wake recirculation bubble. (*b*) Flow regimes for two tandem circular cylinders. From left to right: the extended-body regime, the reattachment regime, and the co-shedding regimes.

4. Discussion: mechanisms that govern the stem dynamics and hydrodynamic forces

In this section, we examine the fundamental flow physics that governs the stem dynamics and the associated hydrodynamic loading within the array. Such analysis provides critical insights into how multiple mechanisms, including shielding, amplification, blockage and oblique-flow effects, as well as delayed flow separation and inter-stem interactions, collectively regulate the magnitude and temporal characteristics of stem motion and the overall hydrodynamic responses.

4.1. *Shielding effect*

When flow encounters a circular cylinder, the near-wake topology can be divided into several canonical regions: an upstream stagnation zone, a boundary layer developing along the cylinder surface, accelerated flow around the lateral sides, and a separated flow containing a small recirculation bubble; see figure 18(*a*) (Zdravkovich 1997). When a second cylinder is placed within the wake of the first, the hydrodynamic loading on the downstream cylinder may be either reduced or enhanced, depending on its position relative to the upstream wake (Sumner 2010). The shielding effect modifies the local dynamic pressure by limiting direct exposure to the freestream. In the low-momentum wake core (region iv), the downstream cylinder experiences reduced stagnation pressure and consequently lower drag, whereas in the high-speed shear layer (region iii), the elevated dynamic pressure results in enhanced drag.

In tandem configurations, the upstream cylinder substantially alters the flow approaching the downstream one, acting as either a turbulence generator or a wake stabiliser (Lee & Basu 1997). Three canonical regimes arise, primarily governed by the spacing ratio s/d, and influenced by Reynolds number and turbulence intensity (Ljungkrona *et al.* 1991; Xu & Zhou 2004; Sumner 2010); see figure 18(*b*). For small spacings ($s/d < 1.2{-}1.8$), the downstream cylinder lies within the vortex-formation region of the upstream cylinder. The upstream shear layers envelop the downstream cylinder without reattachment, and elongated vortices form only behind the downstream body, producing a narrower wake (Lin *et al.* 2002). The nearly stagnant gap flow results in negative mean drag and weak lift fluctuations, representing an extended-body regime with strong shielding (Alam *et al.* 2003). For intermediate spacings ($1.2{-}1.8 < s/d < 3.4{-}3.8$), the upstream shear layers reattach to the downstream cylinder, while vortex shedding remains confined to the downstream body (Zhou & Yiu 2006). Although

https://doi.org/10.1017/jfm.2026.12218 Published online by Cambridge University Press

unsteady gap flow may occur (Igarashi 1981; Kitagawa & Ohta 2008), the mean drag remains negative with relatively small lift fluctuations, indicating weakened but persistent shielding. For larger spacings ($s/d > 3.4{-}3.8$), both cylinders shed vortices. The downstream cylinder is excited by impinging upstream vortices, enhancing its own shedding and accelerating wake dissipation (Zhou & Yiu 2006). In this co-shedding regime, phase-locking causes both cylinders to shed at the same frequency (Zdravkovich 1987; Alam & Zhou 2007). The mean drag becomes positive and approaches the isolated-cylinder value, accompanied by large force fluctuations due to the elevated dynamic pressure induced by the incoming vortices (Alam *et al.* 2003).

The shielding effect represents a key mechanism of flow–structure interference that modulates hydrodynamic loading, energy transfer and multiscale flow coherence within arrays of aquatic vegetation. Upstream elements attenuate both the mean velocity and turbulence intensity inside the canopy (figures 10 and 13), causing the flow to transition from the high-speed mixing layer above the canopy to a low-speed, vortex-dominated region characteristic of a von Kármán vortex street within the canopy (Poggi *et al.* 2004). In this region, the mean drag on downstream elements is substantially reduced relative to that of an isolated cylinder.

The shielding effect exhibits strong vertical variation, spanning from shear-layer reattachment to direct vortex impingement. Near the bed, where the local velocity is low, the shear layers shed from the front-row stems remain coherent over long streamwise distances. Their persistent coherence strengthens hydrodynamic shielding, suppresses the dynamic pressure on downstream cylinders, and consequently reduces the mean drag well below the isolated-cylinder reference (figures 10*a*ii,*c*ii). Moving towards the stem tips, the higher local velocity and larger stem oscillations intensify shear-layer roll-up, promoting earlier vortex shedding (figures 10*b*ii,*b*iii). In this upper region, downstream cylinders experience strong vortex impingement, which generally elevates their mean drag.

The influence of K manifests primarily through changes in stem oscillation amplitude and deformation. For moderately flexible stems ($K = 0.32$), vigorous oscillations promote vortex impingement over nearly the entire stem length (figure 10*b*), thereby altering the form of shielding experienced by downstream elements, from velocity-deficit-driven shielding to shielding characterised by impinging vortices, which can yield elevated mean drag. In contrast, for stiffer and more flexible cases, stem oscillation remains small, and shear-layer reattachment is more commonly observed across the vertical extent, especially around the front-row cylinders (figures 10*a*,*c*,*d*). It should be noted that for pairs of oscillating cylinders, their relative phase may significantly affect the instantaneous and mean hydrodynamic forces (Alam & Zhou 2007). However, such phase-dependent effects are not considered in the present force-based discussion.

4.2. *Delayed separation mechanism*

The separation characteristics of bluff bodies play a central role in determining hydrodynamic loading. For a rigid circular cylinder at moderate to high Reynolds numbers, the drag coefficient is governed primarily by the separation angle because the flow detachment determines both the wake width and leeward pressure deficit (Schewe 1983; Zdravkovich 1997; Jiang 2020; Chen & Li 2023). Delayed separation narrows the recirculation region, thereby promoting greater momentum entrainment from the freestream, weakening the pressure difference across the body, and ultimately reducing the drag (Achenbach 1968; Achenbach & Heinecke 1981; Zdravkovich 1997; Wu *et al.* 2004; Jiang 2020). This canonical behaviour provides a useful baseline for understanding flexible stems in turbulent flows.

https://doi.org/10.1017/jfm.2026.12218 Published online by Cambridge University Press

Unlike rigid cylinders, flexible stems undergo flow-induced deformation that passively reconfigures their geometry. As a stem bends downstream, it becomes increasingly aligned with the local flow (Nepf 2012), weakening the adverse pressure gradient, and delaying separation. The reduced projected area suppresses vortex shedding by prolonging shear-layer development and shifting the effective separation point downstream (Chen & Li 2025), thereby reducing both mean drag and fluctuating lift (Box *et al.* 2021; Chen *et al.* 2026*a*).

Within an array, separation delay becomes a collective process governed by the local velocity deficit, wake sheltering, and inter-stem hydrodynamic interactions. Frontal blockage reduces the effective Reynolds number of individual stems, promoting viscous diffusion and delaying separation. Upstream wakes further reduce the incident momentum on downstream stems, alleviating the adverse pressure gradient, increasing the separation angle, and thereby markedly reducing the drag on sheltered stems.

Flexibility induces additional complexity by generating spatially varying reconfiguration along and among stems, leading to spanwise heterogeneous separation behaviour (Chen *et al.* 2026*b*). Regions of strong bending may sustain attached flow, suppressing large-scale vortex formation, and acting as distributed damping that weakens flow-induced forcing across the array. Stem oscillations further modulate the instantaneous curvature and inclination, altering the pressure distribution that governs separation. When the structural natural frequency approaches the vortex-shedding frequency, fluid–structure resonance may occur (Rosti *et al.* 2018), promoting spanwise-coherent bending and further delaying separation.

Overall, delayed separation in flexible stem arrays arises from a synergistic interplay between passive reconfiguration, wake sheltering, reduced effective Reynolds number, and fluid–structure resonance. Together, these mechanisms shape the mean and unsteady loading experienced by both natural vegetation and engineered vegetation-mimicking canopies.

4.3. *Amplification effect*

For an oscillating cylinder, body motion feeds back into the surrounding flow, modifying vortex formation, shedding frequency, and wake topology (Bearman 2011). During VIV, when the oscillation frequency approaches the structural natural frequency, a lock-in regime develops in which vibration amplitude becomes large, and both the mean and fluctuating drag are substantially amplified (Gopalkrishnan 1993; Khalak & Williamson 1999; Govardhan & Williamson 2000). This amplification results from strong flow–structure coupling that reorganises vortex dynamics and alters the instantaneous pressure distribution around the cylinder.

Cylinder motion continuously modulates the effective angle of attack and separation location. The alternating acceleration and deceleration of the near-wake fluid distort the boundary layer, promoting separation, delaying reattachment, and strengthening recirculation. Elevated instantaneous relative velocity (U_R) between the flow and the body intensifies vortex development (figure 19), while oscillatory motion injects additional energy into the wake, enhancing turbulence production and Reynolds stresses. The resulting broadened wake increases the pressure deficit and the form drag, producing larger asymmetric pressure fields, and amplifying both the mean and fluctuating forces.

This mechanism underlies the enhanced mean drag observed in aquatic vegetation arrays. For a circular cylinder, the amplification ratio increases approximately with vibration amplitude, with larger amplitudes producing higher mean drag (Bishop & Hassan 1964; Sarpkaya 1978, 1995; Khalak & Williamson 1999). Flexible aquatic stems

https://doi.org/10.1017/jfm.2026.12218 Published online by Cambridge University Press

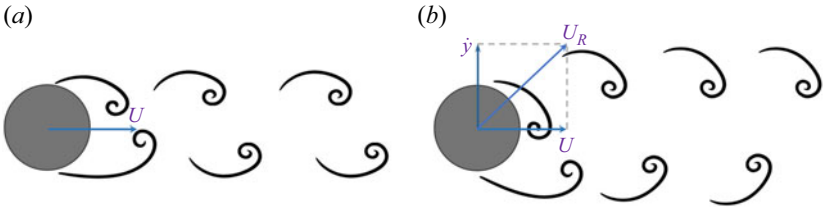


Figure 19. Schematic diagram of the vortex dynamics of (*a*) stationary and (*b*) oscillating circular cylinders. Here, U_R is the relative velocity, which is defined as $U_R = \sqrt{\dot{y}^2 + U^2}$, with $\dot{y}$ denoting the cylinder transverse velocity, and U denoting the oncoming flow velocity.

undergo flow-induced oscillations that increase local drag and modify the bulk hydraulic resistance of the canopy (Luhar & Nepf 2011; Luhar & Nepf 2013; Chen *et al.* 2026*c*). For an individual stem, intermediate flexibility maximises energy dissipation due to resonance-like drag amplification (Chen & Li 2025), and comparable behaviour is observed in stem arrays, as illustrated in figure 14.

4.4. *Blockage effect*

The blockage effect refers to the influence of geometric confinement imposed by channel walls, lateral boundaries or neighbouring obstacles on the flow around an immersed body. It becomes significant when a bluff body occupies a substantial portion of a confined flow passage, thereby modifying the local velocity field. First, the reduced flow area accelerates the fluid, particularly within the gap between the body and the sidewall (Maskell 1965). Second, lateral confinement restricts the natural expansion of the wake, causing it to narrow and reattach closer to the body (Zovatto & Pedrizzetti 2001). Consequently, the vortex shedding frequency typically increases (Zdravkovich 2003). These changes also alter the hydrodynamic loading: drag generally increases because of the higher relative velocity and steeper pressure gradients, while lift is strongly affected by the altered vortex formation (Okamoto & Takeuchi 1975). Under strong confinement, the blockage may even delay or suppress boundary-layer separation (Taneda 1964).

Conceptually, blockage can be viewed as an externally imposed confinement effect generated by surrounding boundaries. By modifying the local dynamic pressure and momentum exchange, it influences both the flow structures and the resulting force coefficients. In the present configuration, the sidewall is located relatively close to the vegetation array. It is reasonable to expect that the confinement accelerates the local flow adjacent to the array, and enhances vortex dynamics in the outer-array region (i.e. between the array edge and the sidewall), as discussed in § 3.3. These effects produce slightly stronger stem motions and modestly higher hydrodynamic loading.

4.5. *Oblique flow effect*

The inclination of a circular cylinder relative to the oncoming flow profoundly alters its vortex dynamics, wake topology and hydrodynamic loading. As illustrated in figure 20(*a*), the incoming flow can be decomposed into a component normal to the cylinder axis and an axial component aligned with the cylinder axis. The normal component drives the formation of spanwise vortices, whereas the axial component disrupts their coherence (Ramberg 1983; Kawamura & Hayashi 1995; Lucor & Karniadakis 2003; Zhou *et al.* 2009). Consequently, vortex shedding becomes fully 3-D and oblique, with spanwise phase differences producing helical or skewed vortices (Shirakashi *et al.* 1986; Wang *et al.* 2019). The enhanced streamwise vorticity generated by the axial flow promotes

https://doi.org/10.1017/jfm.2026.12218 Published online by Cambridge University Press

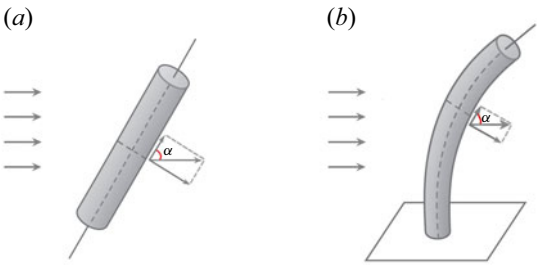


Figure 20. Schematics of the flow past an inclined (*a*) rigid circular cylinder and (*b*) flexible vegetation element. The incoming flow approaches from left to right. The inclination angle α denotes the angle between the freestream direction and the cylinder (or stem) axis.

vortex stretching, reorientation, and more frequent vortex dislocations arising from non-uniform phase distributions (Lucor & Karniadakis 2003; Zhao 2015). These processes weaken the spanwise coherence, and diminish the regularity of the von Kármán vortex street. Because the effective cross-flow velocity decreases with inclination, the shedding frequency generally decreases (Van Atta 1968; Shirakashi *et al.* 1986), accompanied by reduced mean drag and less periodic force fluctuations.

When the inclined cylinder undergoes VIV, the weaker vortices and reduced coherence attenuate the fluctuating lift, and disrupt spanwise synchronisation, leading to desynchronised or partially locked-in responses. For a flexible vegetation element, however, the dynamics becomes more complex. As depicted in figure 20(*b*), the effective inclination angle varies along the stem due to curvature-dependent deformation, producing vertically non-uniform FSIs. The effects of deflection and oscillation for an individual flexible stem have been discussed in Chen & Li (2025). Towards the stem tip, increasing deformation produces a more streamlined configuration, while the oscillation amplitude also increases. Consequently, vortex shedding is governed by the combined effects of deformation and oscillation. Under strong reconfiguration, deformation dominates, and vortices are shed primarily from the tip, approximately aligned with the mean flow. When the stem behaves more rigidly, oscillation dominates, and vortex shedding intensifies towards the tip due to the larger oscillation amplitude. More generally, a flexible inclined cylinder develops highly 3-D, weakly coherent vortex structures because of the combined effects of axial flow and structural deformation, resulting in lower effective cross-flow velocity, reduced drag and lift, and suppressed flow-induced vibration (Chen *et al.* 2026*a*,*b*). These inclination-dependent mechanisms are essential for predicting hydrodynamic loading, wake characteristics and structural responses in engineering and environmental applications.

5. Conclusions

In this study, we investigated the dynamics of flow through a square array of flexible stems with varying flexibility using direct numerical simulations. We analysed the stem response, 3-D vortex dynamics and interactions, and flow distributions within and above the stem arrays. Moreover, we discussed the hydrodynamic drag on the stems, and the distributions of wall shear stress and turbulent kinetic energy. The principal findings of this study can be summarised as follows.

The dynamics of stem arrays is strongly influenced by stem flexibility. Three distinct response regimes are identified within the simulated parameter space. At high K, the stems behave similarly to rigid cylinders, exhibiting only limited deformation and oscillations.

https://doi.org/10.1017/jfm.2026.12218 Published online by Cambridge University Press

At intermediate K, the structural natural frequency matches the oscillation frequency, producing a lock-in regime with the strongest stem response. At low K, stem oscillation becomes moderate, while deformation increases markedly. The array dynamics is more irregular, with higher-mode responses emerging. The evolution of stem displacement further suggests that stem deformation generally increases as K decreases.

The vortex dynamics within and around the stem arrays reveals several interaction mechanisms that explain these response regimes. The intensity of vortical activity reaches its maximum for case $K = 0.32$, corresponding to the largest oscillation amplitude. Both stem oscillation and deformation influence hydrodynamic interactions, which can be broadly classified into two categories: shear-layer reattachment, and vortex–vortex interaction. Shear-layer reattachment promotes pressure balance around the stem circumference and suppresses oscillation, while vortex–vortex interactions enhance vortex shedding, intensify pressure asymmetry, and consequently amplify the stem response.

Flow distributions from multiple perspectives further elucidate the hydrodynamics within the stem arrays. The flow accelerates through the gap between adjacent stem columns, forming jet-like structures, whereas substantially lower velocities develop in the wake of the stems because of shielding. Both stem oscillation and deformation strongly influence the flow structure and vortex dynamics. Stem oscillation increases the flow velocity in the upper region of the array, while reducing the near-bed flow momentum. Stem deformation modifies the spacing between adjacent stems, leading to a vertical transition of the dominant interaction mechanism from vortex–vortex interaction to shear-layer reattachment.

The energy-dissipation and sediment-transport capacities of the stem arrays are evaluated using the hydrodynamic drag together with the spatial distributions of the mean bed shear stress ($\overline{\tau}_b^*$) and root mean square bed friction velocity (u_τ^{SD}). The array with intermediate K exhibits the greatest energy dissipation, surpassing even that of the rigid configuration. The mean bed shear stress reaches its maximum near the upstream edge of the array, and remains appreciable towards the downstream end. Although stem oscillation enhances vortex dynamics, it weakens the near-bed flow, resulting in a lower u_τ^{SD} than that of the relatively rigid cases.

A unified physical framework emerges in which shielding, delayed separation, drag amplification, blockage and oblique-flow effects collectively govern the dynamics of flexible stem arrays and the resulting hydrodynamic loading. By linking flow topology, wake interference and deformation-induced reconfiguration, this framework explains how stem motion and force generation arise from the interplay between velocity-deficit shielding, resonance-like drag amplification, confinement-modified wake dynamics, and inclination-induced 3-D vortex shedding. These coupled mechanisms collectively contribute to determining the mean and unsteady hydrodynamic forces within vegetated canopies, thereby regulating energy dissipation, momentum transport and structural resistance in aquatic environments.

This study provides physical insight into the regime-dependent flow–structure interactions governing hydrodynamic forces, energy dissipation and transport processes within flexible stem arrays. These results further suggest that arrays with intermediate flexibility may provide an effective strategy for enhancing energy dissipation in coastal protection applications.

The present study considers only a regularly spaced, aligned stem array, whereas natural vegetation canopies generally exhibit irregular and spatially heterogeneous distributions. Alternative stem arrangements may alter wake interactions and the formation of high-velocity corridors, thereby affecting vortex lock-in and inducing subtle changes in the near-bed flow.

https://doi.org/10.1017/jfm.2026.12218 Published online by Cambridge University Press

Acknowledgements. This work was supported with computational resources provided by the National Supercomputing Centre, Singapore (https://www.nscc.sg), under project IDs 11003759 and 11004188.

Funding. This project is funded by the Research, Innovation and Enterprise 2025 Coastal Protection and Flood Management Research Programme. The authors are grateful to the National Research Foundation of Singapore, PUB (Singapore's National Water Agency) for supporting this work done in the Coastal Protection and Flood Resilience Institute (CFI) Singapore under the project grant H1-P3.

Declaration of interests. The authors report no conflict of interest.

References

ACHENBACH, E. 1968 Distribution of local pressure and skin friction around a circular cylinder in cross-flow up to $Re = 5 \times 10^6$. *J. Fluid Mech.* **34**, 625–639.

ACHENBACH, E. & HEINECKE, E. 1981 On vortex shedding from smooth and rough cylinders in the range of Reynolds numbers 6×10^3 to 5×10^6. *J. Fluid Mech.* **109**, 239–251.

ACKERMAN, J.D. & OKUBO, A. 1993 Reduced mixing in a marine macrophyte canopy. *Funct. Ecol.* **7**, 305–309.

ALAM, M.M., MORIYA, M., TAKAI, K. & SAKAMOTO, H. 2003 Fluctuating fluid forces acting on two circular cylinders in a tandem arrangement at a subcritical Reynolds number. *J. Wind Engng Ind. Aerodyn.* **91**, 139–154.

ALAM, M.M. & ZHOU, Y. 2007 Phase lag between vortex shedding from two tandem bluff bodies. *J. Fluids Struct.* **23**, 339–347.

ARCEMENT, G.J., SCHNEIDER, V.R. & VERNE, R. 1988 Roughness coefficients for densely vegetated flood plains. U.S. Geological Survey. Available at: https://pubs.usgs.gov/publication/wri834247.

ARMANINI, A. & CAVEDON, V. 2019 Bed-load through emergent vegetation. *Adv. Water Res.* **129**, 250–259.

BEARMAN, P.W. 2011 Vortex shedding from oscillating bluff bodies. *Annu. Rev. Fluid Mech.* **44**, 195–215.

BELCHER, S.E., JERRAM, N. & HUNT, J.C.R. 2003 Adjustment of a turbulent boundary layer to a canopy of roughness elements. *J. Fluid Mech.* **488**, 369–398.

BISHOP, R.E.D. & HASSAN, A.Y. 1964 The lift and drag forces on a circular cylinder oscillating in a flowing fluid. *Proc. R. Soc. Lond. A* **277**, 51–75.

BOX, W., JÄRVELÄ, J. & VÄSTILÄ, K. 2021 Flow resistance of floodplain vegetation mixtures for modelling river flows. *J. Hydrol.* **601**, 126593.

CAROLLO, F.G., FERRO, V. & TERMINI, D. 2005 Flow resistance law in channels with flexible submerged vegetation. *J. Hydraul. Engng* **131** (7), 554–564.

CARPENTER, S.R. & LODGE, D.M. 1986 Effects of submersed macrophytes on ecosystem processes. *Aquat. Bot.* **26**, 341–370.

CHANG, W.Y., CONSTANTINESCU, G. & TSAI, W.F. 2017 On the flow and coherent structures generated by an array of rigid emerged cylinders place in an open channel with flat and deformed bed. *J. Fluid Mech.* **831**, 1–40.

CHANG, W.Y., CONSTANTINESCU, G. & TSAI, W.F. 2020 Effect of array submergence on flow and coherent structures through and around a circular array of rigid vertical cylinders. *Phys. Fluids* **32**, 035110.

CHEN, W., JI, C., XU, W., LIU, S. & CAMPBELL, J. 2015 Response and wake patterns of two side-by-side elastically supported circular cylinders in uniform laminar cross-flow. *J. Fluids Struct.* **55**, 218–236.

CHEN, W., JI, C., ALAM, M.M., XU, D., AN, H., TONG, F. & ZHAO, Y. 2022 Flow-induced vibrations of a D-section prism at a low Reynolds number. *J. Fluid Mech.* **941**, A52.

CHEN, W. & LI, Y.P. 2025 Simulation of a wall-mounted stem in uniform flow. *J. Fluid Mech.* **1013**, A17.

CHEN, W. & LI, Y. 2023 Evidence and physical mechanism for vortex-induced vibration of a bluff body without an afterbody. *Phys. Fluids* **35**, 065143.

CHEN, X., ZHANG, Z., XU, D., JI, C. & GHISALBERTI, M. 2026*a* Static bending effects on interfacial momentum exchange and depth-varying drag in submerged canopies. *Coast. Engng* **211**, 105077.

CHEN, X., XU, D. & JI, C. 2026*b* Numerical study of turbulent aquatic canopy flows in a vegetated channel with flexible stems. *J. Hydrol. Engng* **31** (2), 04026001.

CHEN, X., JI, C., XU, D., DOU, S. & YU, X. 2026*c* Beyond bending: multi-directional vegetation sway as a driver of turbulence and momentum transport in submerged canopies. *Engng Appl. Comput. Fluid Mech.* **20** (1), 2644565.

CHEN, Z., JIANG, C. & NEPF, H. 2013 Flow adjustment at the leading edge of a submerged aquatic canopy. *Water Resour. Res.* **49** (9), 5537–5551.

https://doi.org/10.1017/jfm.2026.12218 Published online by Cambridge University Press

CHENG, Z., KOKEN, M. & CONSTANTINESCU, G. 2018 Approximate methodology to account for effects of coherent structures on sediment entrainment in RANS simulations with a movable bed and applications to pier scour. *Adv. Water Resour.* **120**, 65–82.

COCEAL, O. & BELCHER, S. 2004 A canopy model of mean winds through urban areas. *Q. J. R. Meteorol. Soc.* **130**, 1349–1372.

DAY, J.W. *et al.* 2007 Restoration of the Mississippi Delta: lessons from hurricanes Katrina and Rita. *Science* **315** (5819), 1679–1684.

DIPLAS, P., DANCEY, C.L., CELIK, A.O., VALYRAKIS, M., GREER, K. & AKAR, T. 2008 The role of impulse on the initiation of particle movement under turbulent flow conditions. *Science* **322** (5902), 717–720.

EINSTEIN, H.A. 1942 Formulas for the transportation of bed load. *Trans. Am. Soc. Civil Engng* **107** (1), 561–577.

ETMINAN, V., LOWE, R.J. & GHISALBERTI, M. 2017 A new model for predicting the drag exerted by vegetation canopies. *Water Resour. Res.* **53**, 3179–3196.

FINNIGAN, J. 2000 Turbulence in plant canopies. *Annu. Rev. Fluid Mech.* **32** (1), 519–571.

GHISALBERTI, M. & NEPF, H.M. 2002 Mixing layer and coherent structures in vegetated aquatic flows. *J. Geophys. Res.* **107** (C2), 3-1–3-11.

GHISALBERTI, M. & NEPF, H.M. 2006 The structure of the shear layer in flows over rigid and flexible canopies. *Environ. Fluid Mech.* **6** (3), 277–301.

GHISALBERTI, M. & NEPF, H.M. 2009 Shallow flows over a permeable medium: the hydrodynamics of submerged aquatic canopies. *Transp. Porous Med.* **78** (2), 309–326.

GOPALKRISHNAN, R. 1993 Vortex-induced forces on oscillating bluff cylinders. PhD thesis, Massachusetts Institute of Technology.

GOVARDHAN, R.N. & WILLIAMSON, C.H.K. 2000 Modes of vortex formation and frequency response of a freely vibrating cylinder. *J. Fluid Mech.* **420**, 85–130.

GREEN, E.P. & SHORT, F.T. 2003, *World Atlas of Seagrasses*. University of California Press.

HE, S., LIU, H. & SHEN, L. 2022 Simulation-based study of turbulent aquatic canopy flows with flexible stems. *J. Fluid Mech.* **947**, A33.

HEATHERSHAW, A. & THORNE, P. 1985 Sea-bed noises reveal role of turbulent bursting phenomenon in sediment transport by tidal currents. *Nature* **316** (6026), 339–342.

HUNT, J.C.R., ABELL, C.J., PETERKA, J.A. & WOO, H. 1978 Kinematical studies of the flows around free or surface-mounted obstacles: applying topology to flow visualization. *J. Fluid Mech.* **86** (1), 179–200.

IGARASHI, T. 1981 Characteristics of the flow around two circular cylinders arranged in tandem: 1st report. *Bull. JSME* **24**, 323–331.

JACKSON, G. & WINANT, C. 1983 Effect of a kelp forest on coastal currents. *Cont. Shelf Res.* **2**, 75–80.

JIANG, H. 2020 Separation angle for flow past a circular cylinder in the subcritical regime. *Phys. Fluids* **32**, 014106.

KADLEC, R.H. 1990 Overland flow in wetlands: vegetation resistance. *J. Hydraul. Engng* **116** (5), 691–706.

KAWAMURA, T. & HAYASHI, T. 1995 Computation of flow around a yawed circular cylinder. *JSME Intl J. B* **37**, 229–236.

KHALAK, A. & WILLIAMSON, C.H.K. 1999 Motions, forces and mode transitions in vortex-induced vibrations at low mass-damping. *J. Fluids Struct.* **13**, 813–851.

KIM, H.D., YU, X. & KAPLAN, D. 2024 Steady flow over a finite patch of submerged flexible vegetation. *Water Resour. Res.* **60**, e2023WR035222.

KING, A.T., TINOCO, R.O. & COWEN, E.A. 2012 A $k-\varepsilon$ turbulence model based on the scales of vertical shear and stem wakes valid for emergent and submerged vegetated flows. *J. Fluid Mech.* **701**, 1–39.

KITAGAWA, T. & OHTA, H. 2008 Numerical investigation on flow around circular cylinders in tandem arrangement at a subcritical Reynolds number. *J. Fluids Struct.* **24**, 680–699.

KOKEN, M. & CONSTANTINESCU, G. 2021 Flow structure inside and around a rectangular array of rigid emerged cylinders located at the sidewall of an open channel. *J. Fluid Mech.* **910**, A2.

KOKEN, M. & CONSTANTINESCU, G. 2023 Influence of submergence ratio on flow and drag forces generated by a long rectangular array of rigid cylinders at the sidewall of an open channel. *J. Fluid Mech.* **966**, A5.

LEE, T. & BASU, S. 1997 Nonintrusive measurements of the boundary layer developing on a single and two circular cylinders. *Exp. Fluids* **23**, 187–192.

LEI, J. & NEPF, H. 2021 Evolution of flow velocity from the leading edge of 2-D and 3-D submerged canopies. *J. Fluid Mech.* **916**, A36.

LIN, J.C., YANG, Y. & ROCKWELL, D. 2002 Flow past two cylinders in tandem: instantaneous and averaged flow structure. *J. Fluids Struct.* **16**, 1059–1071.

https://doi.org/10.1017/jfm.2026.12218 Published online by Cambridge University Press

LJUNGKRONA, L., NORBERG, C. & SUNDEN, B. 1991 Free-stream turbulence and tube spacing effects on surface pressure fluctuations for two tubes in an in-line arrangement. *J. Fluids Struct.* **5**, 701–727.
LUCOR, D. & KARNIADAKIS, G.E. 2003 Effects of oblique inflow in vortex-induced vibrations. *Flow Turbul. Combust.* **71**, 375–389.
LUHAR, M., COUTU, S., INFANTES, E., FOX, S. & NEPF, H. 2010 Wave induced velocities inside a model seagrass bed. *J. Geophys. Res.* **115**, C12005.
LUHAR, M. & NEPF, H.M. 2011 Flow–induced reconfiguration of buoyant and flexible aquatic vegetation. *Limnol. Oceanogr.* **56** (6), 2003–2017.
LUHAR, M. & NEPF, H.M. 2013 From the blade scale to the reach scale: a characterization of aquatic vegetative drag. *Adv. Water Resour.* **51**, 305–316.
MASKELL, E.C. 1965 A theory of the blockage effects on bluff bodies and stalled wings in a closed wind tunnel. *Aeronautical Research Council Reports and Memoranda* No. 3400. London: Her Majesty's Stationery Office.
MEYER-PETER, E. & MÜLLER, R. 1948 Formulas for bed load transport. In *Proceedings of the 2nd Meeting of the International Association of Hydraulic Structures Research*, pp. 39–64. International Association for Hydraulic Structures Research.
MONTI, A., OLIVIERI, S. & ROSTI, M.E. 2023 Collective dynamics of dense hairy surfaces in turbulent flow. *Sci. Rep.* **13** (1), 5184.
NEPF, H., GHISALBERTI, M., WHITE, B. & MURPHY, E. 2007 Retention time and dispersion associated with submerged aquatic canopies. *Water Resour. Res.* **43**, W04422.
NEPF, H.M. 2012 Flow and transport in regions with aquatic vegetation. *Annu. Rev. Fluid Mech.* **44** (1), 123–142.
NEPF, H.M. & VIVONI, E.R. 2000 Flow structure in depth-limited, vegetated flow. *J. Geophys. Res.: Oceans* **105** (C12), 28547–28557.
NI, J., JI, C., XU, D., ZHANG, X. & LIANG, D. 2023 On monami modes and scales of a flexible vegetation array in a laminar boundary layer. *Phys. Fluids* **35**, 074113.
NI, J., ZHANG, Z., JI, C., XU, D. & ZHANG, X. 2025 Evolution of large-scale vortices and its influence on flow and flexible vegetation dynamics of a finite-length canopy in a 2-D laminar flow. *J. Fluid Mech.* **1017**, A2.
NICHOLAS, S., OMIDYEGANEH, M. & PINELLI, A. 2022 Numerical investigation of regime transition in canopy flows. *Flow Turbul. Combust.* **109**, 1133–1153.
OKAMOTO, T., NEZU, I. & SANJOU, M. 2016 Flow-vegetation interactions: length-scale of the 'monami' phenomenon. *J. Hydraul. Res.* **54** (3), 251–262.
OKAMOTO, T. & TAKEUCHI, M. 1975 Effect of side walls of wind tunnel on flow around two-dimensional circular cylinder and its wake. *Bull. JSME* **18**, 1011–1017.
PAPAIOANNOU, G.V., YUE, D.K.P., TRIANTAFYLLOU, M.S. & KARNIADAKIS, G.E. 2006 Three-dimensionality effects in flow around two tandem cylinders. *J. Fluid Mech.* **558**, 387–413.
PESKIN, C.S. 1972 Flow patterns around heart valves: a digital computer method for solving the equations of motion. PhD thesis, Yeshiva University.
POGGI, D., PORPORATO, A., RIDOLFI, L., ALBERTSON, J. & KATUL, G. 2004 The effect of vegetation density on canopy sub-layer turbulence. *Boundary-Layer Meteorol.* **111** (3), 565–587.
PUJOL, D., SERRA, T., COLOMER, J. & CASAMITJANA, X. 2013 Flow structure in canopy models dominated by progressive waves. *J. Hydrol.* **486**, 281–292.
RAMBERG, S.E. 1983 The effects of yaw and finite length upon the vortex wakes of stationary and vibrating circular cylinders. *J. Fluid Mech.* **128**, 81–107.
RAUPACH, M., FINNIGAN, J. & BRUNET, Y. 1996 Coherent eddies and turbulence in vegetation canopies: the mixing layer analogy. *Boundary-Layer Meteorol.* **78**, 351–382.
ROMINGER, J.T. & NEPF, H.M. 2011 Flow adjustment and interior flow associated with a rectangular porous obstruction. *J. Fluid Mech.* **680**, 636–659.
ROSTI, M.E., BANAEI, A.A., BRANDT, L. & MAZZINO, A. 2018 Flexible fiber reveals the two-point statistical properties of turbulence. *Phys. Rev. Lett.* **121**, 044501.
ROTA, G.F., MONTI, A., OLIVIERI, S. & ROSTI, M.E. 2024 Dynamics and fluid–structure interaction in turbulent flows within and above flexible canopies. *J. Fluid Mech.* **989**, A11.
SAHA, A.K. 2013 Unsteady flow past a finite square cylinder mounted on a wall at low Reynolds number. *Comput. Fluids* **88**, 599–615.
SAND-JENSEN, K. 1998 Influence of submerged macrophytes on sediment composition and near-bed flow in lowland streams. *Freshwater Biol.* **39** (4), 663–679.
SARPKAYA, T. 1978 Fluid forces on oscillating cylinders. *ASCE J. Waterway Port Coastal Ocean Div.* **104**, 275–290.

https://doi.org/10.1017/jfm.2026.12218 Published online by Cambridge University Press

SARPKAYA, T. 1995 Hydrodynamic damping, flow-induced oscillations, and biharmonic response. *ASME J. Offshore Mech. Arctic Engng* **117**, 232–238.
SCHEWE, G. 1983 On the force fluctuations acting on a circular cylinder in crossflow from subcritical up to transcritical Reynolds numbers. *J. Fluid Mech.* **133**, 265–285.
SCHULZ, M., KOZERSKI, H.-P., PLUNTKE, T. & RINKE, K. 2003 The influence of macrophytes on sedimentation and nutrient retention in the lower River Spree (Germany). *Water Res.* **37** (3), 569–578.
SHAN, Y., ZHAO, T., LIU, C. & NEPF, H. 2020 Turbulence and bed load transport in channels with randomly distributed emergent patches of model vegetation. *Geophys. Res. Lett.* **47** (12), e2020GL087055.
SHIELDS, A. 1936 Anwendung der Ähnlichkeitsmechanik und der Turbulenzforschung auf die Geschiebebewegung. Mitteilungen der Preußischen Versuchsanstalt für Wasserbau und Schiffbau, Heft 26 (In German), p. 26. Preußische Versuchsanstalt für Wasserbau und Schiffbau.
SHIH, C., WANG, Y.K. & TING, E.C. 2004 Fundamentals of a vector form intrinsic finite element. Part III: Convected material frame and examples. *J. Mech.* **20** (2), 133–143.
SHIH, W. & DIPLAS, P. 2018 A unified approach to bed load transport description over a wide range of flow conditions via the use of conditional data treatment. *Water Resour. Res.* **54** (5), 3490–3509.
SHIRAKASHI, M., HASEGAWA, A. & WAKIYA, S. 1986 Effect of the secondary flow on Karman vortex shedding from a yawed cylinder. *JSME Intl J. B* **51**, 1124–1128.
SINGH, R., BANDI, M.M., MAHADEVAN, A. & MANDRE, S. 2016 Linear stability analysis for monami in a submerged seagrass bed. *J. Fluid Mech.* **786**, R1.
SRIRAM, V., STOESSER, T., YAN, S. & MURALI, K. 2023 *Hydrodynamics of Wave–Vegetation Interactions*. World Scientific.
SUMER, B.M., CHUA, L.H.C., CHENG, N.-S. & FREDSØE, J. 2003 Influence of turbulence on bed load sediment transport. *J. Hydraul. Engng* **129** (8), 585–596.
SUMNER, D. 2010 Two circular cylinders in cross-flow: a review. *J. Fluids Struct.* **26**, 849–899.
TANEDA, S. 1964 Experimental investigation of the wall-effect on a cylindrical obstacle moving in a viscous fluid at low Reynolds number. *J. Phys. Soc. Japan* **19**, 1024–1030.
TEMMERMAN, S., MEIRE, P., BOUMA, T.J., HERMAN, P.M., YSEBAERT, T. & DE VRIEND, H.J. 2013 Ecosystem-based coastal defence in the face of global change. *Nature* **504**, 79–83.
THAPA, J., ZHAO, M., ZHOU, T. & CHENG, L. 2014 Three-dimensional simulation of vortex shedding flow in the wake of a yawed circular cylinder near a plane boundary at a Reynolds number of 500. *Ocean Engng* **87**, 25–39.
THOMPSON, G.T. & ROBERSON, J.A. 1976 A theory of flow resistance for vegetated channels. *Trans. ASAE* **19** (2), 0288–0293.
TING, E.C., DUAN, Y.F. & WU, D.Y. 2012 *Vector Mechanics of Structures (in Chinese)*. Science Press.
TING, E.C., SHIH, C. & WANG, Y.-K. 2004*a* Fundamentals of a vector form intrinsic finite element. Part I. Basic procedure and a plane frame element. *J. Mech.* **20** (2), 113–122.
TING, E.C., SHIH, C. & WANG, Y.-K. 2004*b* Fundamentals of a vector form intrinsic finite element. Part II. Plane solid elements. *J. Mech.* **20** (2), 123–132.
TING, E.C. & WANG, C.Y. 2008 Vector mechanics of solids. *Research report*, National Central University, Taiwan (in Chinese).
TINOCO, R.O. & COCO, G. 2014 Observations of the effect of emergent vegetation on sediment resuspension under unidirectional currents and waves. *Earth Surf. Dyn.* **2** (1), 83–96.
TINOCO, R.O. & COCO, G. 2016 A laboratory study on sediment resuspension within arrays of rigid cylinders. *Adv. Water Resour.* **92**, 1–9.
TINOCO, R.O. & COCO, G. 2018 Turbulence as the main driver of resuspension in oscillatory flow through vegetation. *J. Geophys. Res.* **123**, 891–904.
TINOCO, R.O. & COWEN, E.A. 2013 The direct and indirect measurement of boundary stress and drag on individual and complex arrays of elements. *Exp. Fluids* **54** (4), 1–16.
TSCHISGALE, S., LÖHRER, B., MELLER, R. & FRÖHLICH, J. 2021 Large eddy simulation of the fluid–structure interaction in an abstracted aquatic canopy consisting of flexible blades. *J. Fluid Mech.* **916**, A43.
TSENG, C. & TINOCO, R.O. 2021 A two-layer turbulence-based model to predict suspended sediment concentration in flows with aquatic vegetation. *Geophys. Res. Lett.* **48** (3), e2020GL091255.
TU, J., YEOH, G.H. & LIU, C. 2018 *Computational Fluid Dynamics: A Practical Approach*. Butterworth-Heinemann.
UNSWORTH, R.K.F., CULLEN-UNSWORTH, L.C., JONES, B.L.H. & LILLEY, R.J. 2022 The planetary role of seagrass conservation. *Science* **377** (6606), 609–613.
VAN ATTA, C.W. 1968 Experiments on vortex shedding from yawed circular cylinders. *AIAA J.* **6**, 931–933.

https://doi.org/10.1017/jfm.2026.12218 Published online by Cambridge University Press

VIEIRA, G.S., ALLSHOUSE, M.R. & MAHADEVAN, A. 2023 Seagrass deformation affects fluid instability and tracer exchange in canopy flow. *Sci. Rep.* **13**, 3910.
WANG, J., HE, G., DEY, S. & FANG, H. 2022*a* Fluid–structure interaction in a flexible vegetation canopy in an open channel. *J. Fluid Mech.* **951**, A41.
WANG, J., HE, G., DEY, S. & FANG, H. 2022*b* Influence of submerged flexible vegetation on turbulence in an open-channel flow. *J. Fluid Mech.* **947**, A31.
WANG, R., CHENG, S. & TING, D.S.K. 2019 Effect of yaw angle on flow structure and cross-flow force around a circular cylinder. *Phys. Fluids* **31**, 01410.
WANG, X., GUALTIERI, C. & HUAI, W. 2023 Grain shear stress and bed-load transport in open channel flow with emergent vegetation. *J. Hydrol.* **618**, 129204.
WILCOCK, R.J., CHAMPION, P.D., NAGELS, J.W. & CROKER, G.F. 1999 The influence of aquatic macrophytes on the hydraulic and physico-chemical properties of a New Zealand lowland stream. *Hydrobiologia* **416**, 203–214.
WONG, C.Y.H., TRINH, P.H. & CHAPMAN, S.J. 2020 Shear-induced instabilities of flows through submerged vegetation. *J. Fluid Mech.* **891**, A17.
WU, C., WU, S., WU, X., ZHANG, Y., FENG, K., ZHANG, W. & ZHAO, Y. 2023 Hydrodynamics affected by submerged vegetation with different flexibility under unidirectional flow. *Front. Mar. Sci.* **9**, 1041351.
WU, F.C., SHEN, H.W. & CHOU, Y.J. 1999 Variation of roughness coefficients for unsubmerged and submerged vegetation. *J. Hydraul. Engng* **125** (9), 934–941.
WU, M.H., WEN, C.Y., YEN, R.H., WENG, M.C. & WANG, A.B. 2004 Experimental and numerical study of the separation angle for flow around a circular cylinder at low Reynolds number. *J. Fluid Mech.* **515**, 233–260.
XU, G. & ZHOU, Y. 2004 Strouhal numbers in the wake of two inline cylinders. *Exp. Fluids* **37**, 248–256.
XU, Y. & NEPF, H. 2020 Measured and predicted turbulent kinetic energy in flow through emergent vegetation with real plant morphology. *Water Resour. Res.* **56** (12), e2020WR027892.
YAGER, E.M. & SCHMEECKLE, M.W. 2013 The influence of vegetation on turbulence and bed load transport. *J. Geophys. Res.* **118** (3), 1585–1601.
YANG, J.Q., CHUNG, H. & NEPF, H.M. 2016 The onset of sediment transport in vegetated channels predicted by turbulent kinetic energy. *Geophys. Res. Lett.* **43** (21), 11261–11268.
YANG, J.Q. & NEPF, H.M. 2018 A turbulence-based bed-load transport model for bare and vegetated channels. *Geophys. Res. Lett.* **45** (19), 10428–10436.
YANG, J.Q. & NEPF, H.M. 2019 Impact of vegetation on bed load transport rate and bedform characteristics. *Water Resour. Res.* **55** (7), 6109–6124.
YANG, L.J., ZHANG, J., QI, W.G. & LI, Y.P. 2025 A phenomenological model for predicting bedload transport in vegetated channels using near-bed turbulent kinetic energy. *Phys. Fluids* **37** (10), 105113.
ZDRAVKOVICH, M.M. 1987 The effects of interference between circular cylinders in cross flow. *J. Fluids Struct.* **1**, 239–261.
ZDRAVKOVICH, M.M. 1997 *Flow Around Circular Cylinders*, Fundamentals, vol. 1. Oxford University Press.
ZDRAVKOVICH, M.M. 2003 *Flow Around Circular Cylinders*, Applications, vol. 2. Oxford University Press.
ZHANG, J., LEI, J., HUAI, W. & NEPF, H. 2020 Turbulence and particle deposition under steady flow along a submerged seagrass meadow. *J. Geophys. Res.: Oceans* **125** (5), e2019JC015985.
ZHANG, J., WANG, P., LI, Z., GUO, M., LI, P., XU, G., YU, K. & WANG, W. 2024 Modeling the transport and mixing of suspended sediment in ecological flows with submerged vegetation: a random displacement model-based analysis. *J. Hydrol.* **645**, 132210.
ZHAO, M. 2015 The validity of the independence principle applied to the vortex-induced vibration of an inclined cylinder in steady flow. *Appl. Ocean Res.* **53**, 155–160.
ZHAO, T. & NEPF, H.M. 2021 Turbulence dictates bedload transport in vegetated channels without dependence on stem diameter and arrangement. *Geophys. Res. Lett.* **48** (21), 1–11.
ZHAO, K., CHENG, N.-S., WANG, X. & TAN, S.K. 2013 Measurements of fluctuation in drag acting on rigid cylinder array in open channel flow. *J. Hydraul. Engng* **140** (1), 48–55.
ZHOU, T., RAZALI, S.F.M., ZHOU, Y., CHUA, L.P. & CHENG, L. 2009 Dependence of the wake on inclination of a stationary cylinder. *Exp. Fluids* **46**, 1125–1138.
ZHOU, Y. & YIU, M.W. 2006 Flow structure, momentum and heat transport in a two-tandem-cylinder wake. *J. Fluid Mech.* **548**, 17–48.
ZOVATTO, L. & PEDRIZZETTI, G. 2001 Flow about a circular cylinder between parallel walls. *J. Fluid Mech.* **440**, 1–25.

https://doi.org/10.1017/jfm.2026.12218 Published online by Cambridge University Press